Morphing Wing Team Spring 2006 Report

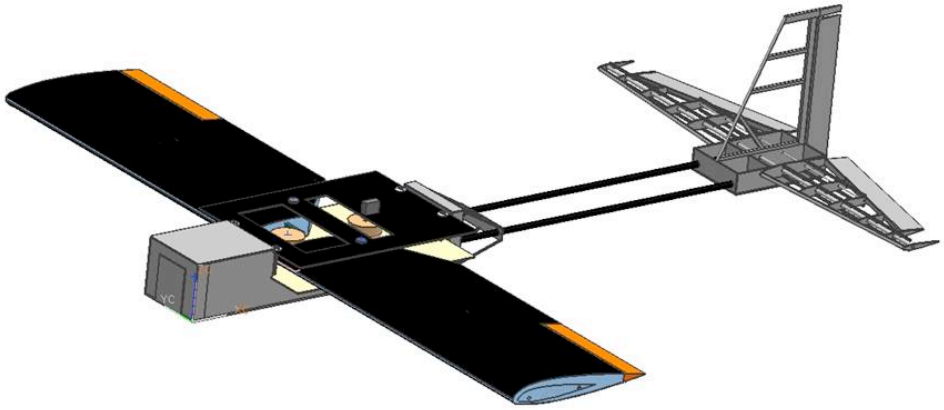

Kevin Dean
Derek DeStephen
James Hotsko, Jr.
Rob Hunsberger
Caroline Hutchison
Kaitlin Keim
Devon Murphy
Meghan Rodwell
Sade Sparbanie
William St. George

Aerospace and Mechanical Engineering
Virginia Tech
8 May 2006

Morphing Wing Team Spring 2006 Report

Kevin Dean
Derek DeStephen
James Hotsko, Jr.
Rob Hunsberger
Caroline Hutchison
Kaitlin Keim
Devon Murphy
Meghan Rodwell
Sade Sparbanie
William St. George

Aerospace and Mechanical Engineering
Virginia Tech
8 May 2006

Summary

During the Spring 2006 semester, the 2005-2006 Morphing Wing senior design team continued work towards the design of a new morphing wing plane. The team completed repairs on the Plane of Substance (POS), performed a single-degree-of-freedom wind tunnel experiment, and flew again in Salem, VA. In addition, the team designed, built, and performed theoretical analysis on a new plane, the Morphing Wing Plane 2006 (MWP-06). A plan is in place to fly MWP-06 before graduation. Lessons learned from this semester will aid in future projects.

Table of Contents

Introduction

This report outlines the work the 2005-2006 Morphing Wing senior design team has completed during the Spring 2006 term. At the outset of this semester, our first goal was to repair and fly the POS a second time; this was accomplished. Our second goal was to design, construct, test, and fly a new morphing wing aircraft. While the original plan was to have symmetric sweep and asymmetric span extension, this plane has both symmetric sweep and span extension. MWP-06 has been designed, built, and computationally analyzed. In addition, MWP-06 will be flown before graduation.

An Overview of Morphing Wing Aircraft

This section presents a history of morphing wing aircraft as well as the benefits of in-flight morphing. In designing traditional aircraft, one must consider the desired speed, altitude, and range of the airplane. Several aircraft have been optimized for various capabilities such as achieving the fastest velocity, maximizing flight capabilities at extreme altitudes, and circling the world without refueling. Despite these accomplishments, very few aircraft demonstrate superior performance in all three areas. As both military and civilian agencies begin to demand a variety of flight capabilities for a single aircraft, airplanes will be required to morph during flight. The world is moving towards creating aircraft that have smooth changes in their physical shape, thus creating desirable flight characteristics as mission requirements become more complex. The benefits of morphing wing aircraft are presented, followed by examples of past advancements in the world of morphing wing aircraft including the F-14 Tomcat, the B-1B Lancer, the AFTI/F-111 Mission Adaptive Wing (MAW), and the F-18/A Active Aeroelastic Wing (AAW).

The Benefits of Morphing Wing Aircraft

Morphing provides the desirable aspects of multiple planes integrated into one structure. Some morphing capabilities currently being explored in industry include variable sweep, camber change, and wing extension. The benefits of variable sweep are maneuverability and roll control while wing extension provides increased lift and decreased fuel consumption during loiter. Span extensions can morph either symmetrically or asymmetrically. Symmetric wing sweep provides additional wing area, allowing an aircraft to loiter and to consume less fuel by mimicking a sailplane. Asymmetric wing sweep allows for roll control while the extensions are out. Wing extensions limit roll authority based on the lack of control surfaces on the outboard surfaces of the wing extensions. Sweep creates a leading edge vortex that helps reduce the onset of separation, which offsets stall. Moreover, sweep at higher airspeeds creates more stability.

The F-14 Tomcat – Swing Wing

The F-14 Tomcat, presented in Figure 1, has wings that are programmed to sweep between 20 and 68 degrees during flight. In storage, the wing can be further swept to 75 degrees. The variable sweep allows for the aircraft to take off in short distances in the non-swept positions and to reach the speed of sound in the swept positions [Swing, 2005].

Figure 1. The F-14 Tomcat [Swing, 2005].

The B-1B Lancer

The B-1B Lancer, shown in Figure 2, also uses a swing wing design allowing for greater range and higher low altitude speeds. The full-forward wing position allows for a short take off and a fast base profile for airfields under attack. The wings can then be positioned for maximum cruise or high speeds in flight. The B-1B holds records for speed, payload, and distance [B-1B, 1997].

Figure 2. The B-1B Lancer [B-1B, 1997].

The AFTI/F-111 – Mission Adaptive Wing (MAW)

The design of the AFTI/F-111, presented in Figure 3, was among the first attempts to change the wing camber smoothly. The performance of the aircraft was improved by optimizing the airfoil to meet each of the flight characteristics demanded for specific missions. The leading edge of the wing is able to travel from +2 to -21 degrees, and the trailing edge from +4 to -22 degrees. Actuation links and hydraulic servo systems control the variable camber of the wing [F-111, 1998].

Figure 3. The AFTI/F-111 – Mission Adaptive Wing [F-111, 1998].

The F/A-18A – Active Aeroelastic Wing (AAW)

The modified F/A-18A fighter, depicted in Figure 4, is capable of supersonic flight and uses thin wings with the theory of wing warming to control the aircraft. The AAW allows the aircraft to have wings that are 15 percent lighter than a conventional wing and generates more torque than conventional flaps alone. This holds true even though the maximum wing twist range is 4 degrees. This aircraft can roll better under high-speed conditions. Moreover, the F/A-18A has decreased weight, drag, and fuel consumption with an increased range [F/A-18, 2000].

Figure 4. The F/A-18A—AAW [F/A-18, 2000].

An Overview of the Continued Work on the POS

After the Fall 2005 semester, the team continued work on the POS after the flight, and subsequent crash of the POS. This semester, repairs were made, a single-degree-of-freedom experiment was performed in the wind tunnel, and a second Salem flight was done. Unfortunately, complications in this flight caused the POS to crash a second time and the damage incurred was beyond repair. The following subsections discuss the status of the POS at the beginning of the Spring 2006 semester, the repairs completed, the flight and the crash.

Initial Status of the POS

At the beginning of the Spring 2006 semester, the POS was not flight ready; the repairs necessary are discussed in this section. The manner in which the wings were connected to the wing box was fixed. The engine cover and fuel tank mount were rebuilt and the wing covers

were removed. The hole created by the wing entering the side of the fuselage upon impact was recovered with balsa sheeting. For both wings, the first and second plywood ribs were replaced. The front landing gear was bent back to its original condition.

Several control changes were made after the first flight. The team realized the stabilator was extremely sensitive and small deflections produced very large moments. To limit the longitudinal control, the throw was limited to 50% of its normal deflection. With this change, the wild pitching experienced during the fall flight was eliminated. In order to increase roll control, the servos controlling the ailerons and flaps were moved to the outside of the wings. In addition, a non-flexible pushrod was used for actuation in place of the flexible cable used during the fall semester; this also reduced the friction experienced between the flexible cable and the tubing inside the wing. After all repairs were made to the POS, the original wind tunnel mount was modified to allow for freedom along the pitching axis of the plane.

Wind Tunnel Experimentation

The team revisited the wind tunnel with the POS in the spring semester; no data was taken during this session. Our goal during this experiment was to see if the aircraft could be trimmed about the longitudinal axis. The aircraft was tested at speeds up to 50 mph and we were able to successfully trim after limiting the throw on the stabilator. At higher speeds a significant flutter was noticed on the vertical tail. As a result, the base of the tail was reinforced in hopes of reducing tail vibration during flight.

A Second Flight in Salem, Virginia

After the successful wind tunnel experiment, the team was ready to fly the POS for a second time. After arriving at the Roanoke Valley RC Club Field in Salem, VA, on March 29,

the plane was assembled. At 7:30am, we began the first of two flights for the day. The first flight lasted approximately 10 seconds and ended with a crash that damaged the first ribs and sweep supports for both wings. The damage to the wings was repaired using fast curing epoxy. The rod on which the sweeping mechanism traveled was also bent in the crash, preventing the use of sweep in the next flight.

The second flight began at 8:55am. After takeoff, the pilot began a slow right turn in order to bring the plane parallel to the airfield. The POS was flying with the wind and towards a nearby business, Timber Truss Housing Systems, Inc. Approximately halfway through this flight, a second right-hand turn was attempted in an effort to bring the plane over the airstrip. The plane did not respond to the pilot's attempts to maneuver. Immediately thereafter the supports connecting the wing box and fuselage failed; this failure happened almost directly over the Timber Truss building. Despite the pilot's attempts to maintain control over the engine, the throttle continued to operate. As a result, the fuselage continued moving at a speed of approximately 60-70 mph over the Timber Truss building, while the separated wings fell to the ground. This impact was obstructed by the building and was not observed by the team. The team immediately drove over to the area to assess the damage. The damage sustained by the POS was beyond repair. In addition, the plane impacted a Timber Truss employee's vehicle, causing significant damage. Virginia Tech's Risk Management Department was contacted and progress towards resolution of repair costs is underway.

An Overview of MWP-06

The team split up into three subgroups—tail, fuselage, and wings—to design and construct MWP-06. Each subgroup took the designs of the other two subgroups into

consideration when making their design decisions. As a result, a complete morphing aircraft was designed, as shown in Figure 5. The following subsections outline the designs and construction process for each of the three subgroups. In addition, the actuation methods used to morph MWP-06 are discussed. Finally, the total cost of this semester's work is presented.

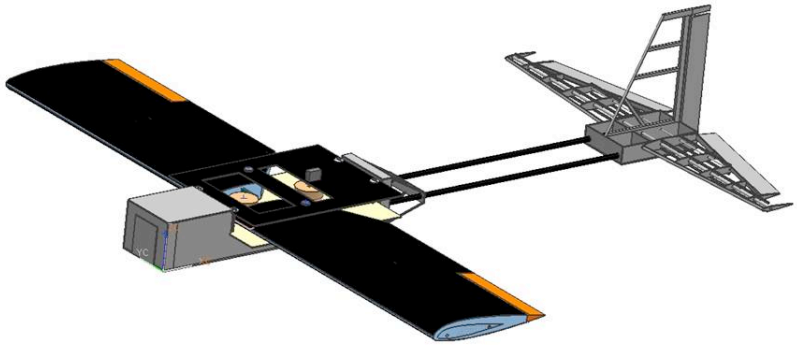

Figure 5. A complete CAD model of MWP-06.

MWP-06 Subgroups

Tail. A conventional tail design was chosen because of its proven reliability and ease of construction. Additionally, the team decided to keep the tail simple so that more time could be spent on designing the actuation systems for the morphing motions.

For the horizontal tail, a NACA 0012 airfoil was selected. This symmetric airfoil is usually used on the horizontal tail of comparable aircraft due to its low pitching moment and ease of construction. For the vertical tail, a flat plate was chosen for two reasons: lift is not required and it is simple to construct. To reduce drag, the leading edge was rounded, and the trailing edge was tapered to a point.

The tail taper and aspect ratio for the horizontal and vertical surfaces were determined using typical values for fighter jets and sailplanes (Raymer, 1989). Fighter jet values were studied because the wings sweep back in flight while sailplane values were examined due to the fact that MWP-06 has extending wings. A summary of these values can be seen in Table 1. For the horizontal tail, the team chose an aspect ratio of 4.48 and taper ratio of 0.4. Values of 1.4 and 0.5, respectively, were chosen for the vertical tail.

Table 1. Typical fighter jet and sailplane ratios.

	Horizontal Tail (HT)		Vertical Tail (VT)	
	AR, Aspect Ratio	_, Taper Ratio	*AR*, Aspect Ratio	_, Taper Ratio
Fighter	3-4	0.2-0.4	0.6-1.4	0.2-0.4
Sailplane	6-10	0.3-0.5	1.5-2.0	0.4-0.6

An initial estimation of the tail size was determined using tail volume coefficients. This method uses typical values of similar aircraft to estimate the tail volume coefficient for the vertical and horizontal tails. It then calculates the area of the tail surfaces using previously estimated geometric values of the wing (Raymer, 1989).

The tail volume coefficients for similar aircraft are listed in Table 2. As previously mentioned, a sailplane was examined because of the wing extensions while a fighter jet was researched due to the wing sweep actuation. In addition, a homebuilt was studied because MWP-06 was going to be built by amateurs. The coefficients listed in Table 2 were used to determine the surface area for the vertical and horizontal tails. The largest tail volume created for any of these coefficients was used to design for the worst case scenario. The surface area of horizontal tail was determined with equation 1:

$$S_{HT} = \frac{c_{HT}\overline{C_W}S_W}{L_{HT}}, \tag{1}$$

where c_{HT} is the horizontal tail volume coefficient, $\overline{C_W}$ is the mean aerodynamic chord of the wing, S_W is the planform area of the wing, and L_{HT} is the distance between quarter chord of the wing at the mean aerodynamic chord to the quarter chord of the mean aerodynamic chord of the tail. The surface area of the vertical tail was found using equation 2:

$$S_{VT} = \frac{c_{VT} b_W S_W}{L_{VT}}, \tag{2}$$

where c_{VT} is the vertical volume coefficient, b_W is the semi-span of the wing, S_W is the planform area of the wing, and L_{VT} is the distance between the quarter chord of the wing at the mean aerodynamic chord to the quarter chord of the vertical tail at the mean aerodynamic chord.

Table 2. Typical Tail Coefficient Values

	Horizontal c_{HT}	**Vertical c_{VT}**
Sailplane	0.50	0.02
Homebuilt	0.50	0.04
Jet Fighter	0.70	0.07

Using the method outlined above, the parameters presented in Table 3 were set for the design of both the horizontal and vertical tail surfaces. The final design has zero sweep at the quarter chord of the horizontal tail surface so a straight carbon fiber spar could be utilized. Due to the taper ratio, the design resulted in a leading edge sweep of 4.4 degrees for the horizontal tail. In designing the vertical tail, the team decided to have three of the edges perpendicular to each other to aid in construction. Due to its taper ratio, the leading edge of the vertical tail is swept back at 26 degrees. The overall sizing can be seen in Figures 6 and 7.

Table 3. Design Parameters used to Geometrically Shape the Tail.

Taper Ratio, Horizontal Tail	_HT	0.4
Taper Ratio, Vertical Tail	_VT	0.5
Aspect Ratio, Horizontal Tail	AR_{HT}	4.48
Aspect Ratio, Vertical Tail	AR_{VT}	1.4
Mean Aerodynamic Chord of Wing	$\overline{C_w}$	12 in.
Semi-span Length of the Wing	b_W	37 in
Wing Area	S_W	172 in^2
Length	L_{HT}	3.4 ft
Length	L_{VT}	3.6 ft
Horizontal Tail Area	S_{HT}	170 in^2
Vertical Tail Area	S_{VT}	76 in^2

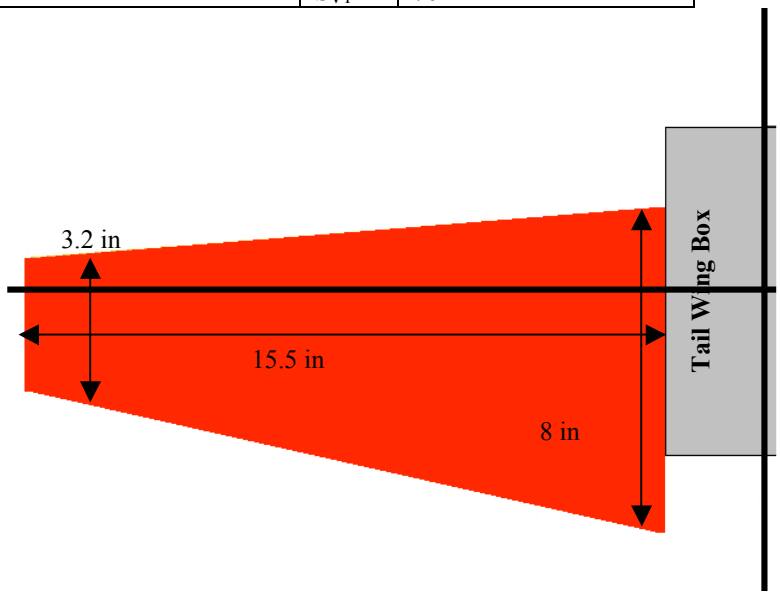

Figure 6. Horizontal Tail Surface

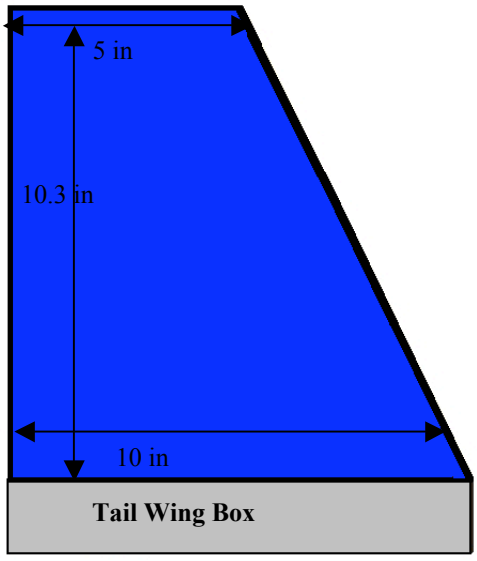

Figure 7. Vertical Tail Surface

To connect the fuselage to the tail surfaces, the team decided to use two half inch hollow carbon fiber tubes, extending from the fuselage and connecting into a tail wing box. These tubes were spaced four inches apart—far enough apart to reduce the effects of torsion, yet close enough to minimize the size of the main fuselage. The tail boom length was determined by the fuselage length.

The tail wing box sizing was determined by the required structure. The initial sizing estimate assumed that the tail would require three bulkheads perpendicular to the tubes. The length of the box was set to eight inches to ensure a strong structure. The width of the box was set to five inches so there would be a half inch on either side of the tubes for strength. The box height was set to two inches. This was determined by the height of the tubes at the entrance of the box. The tail wing box, as presented in Figure 8, was constructed with aircraft grade plywood and balsa wood.

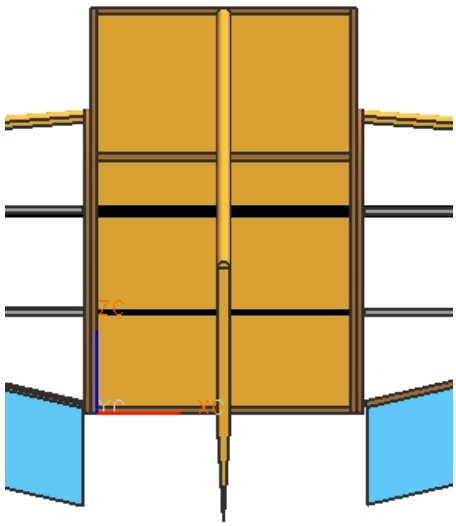

Figure 8. A CAD drawing of the tail wingbox.

The control surfaces were sized as suggested by Raymer. They begin at the fuselage, extend to about ninety percent of the tail span, and are tapered in line with the vertical and

horizontal surfaces. The rudder and elevator have constant chords. It is typical to size the rudder and elevator to be approximately twenty-five to fifty percent of the tail chord. Therefore, the rudder is 9.8 by 2 inches and the two elevators are 13.25 by 1.75 inches.

The construction method used for the horizontal tail surface was a traditional built up structure consistent with Radio Controlled (R/C) designs. There were six basswood ribs, cut using a LaserCamm for accuracy and precision, which run along the span of each side of the horizontal tail surface. The elevator was constructed from solid balsa. Figure 9 shows the horizontal tail.

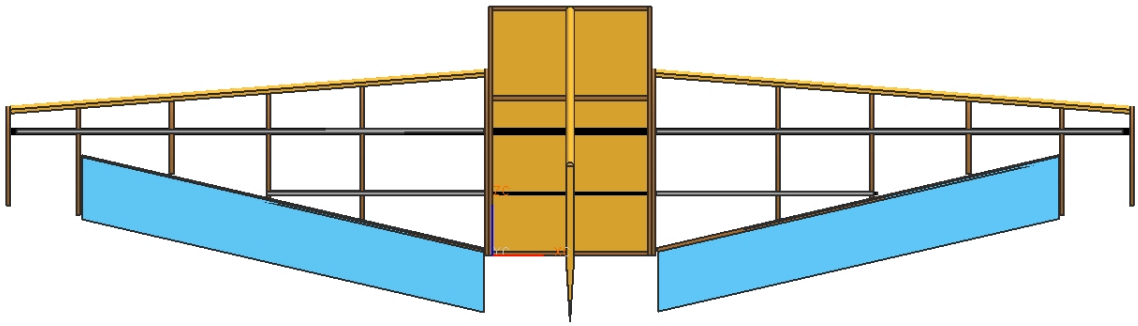

Figure 9. A CAD drawing of the horizontal tail surface.

The vertical tail surface also used a traditional built up structure. The ribs, leading edge, trailing edge, and rudder were constructed with balsa. The vertical tail is shown in Figure 10. After construction of the tail was completed, the fully assembled structure was covered with Monokote®.

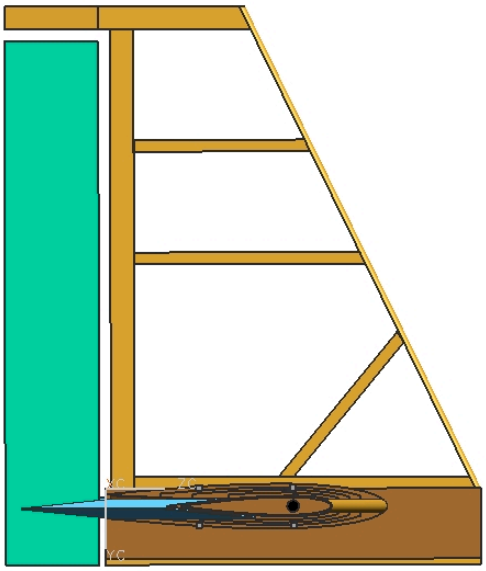

Figure 10. The vertical tail surface.

Fuselage. MWP-06's fuselage is more user-friendly and structurally sound than that of the POS. The fuselage was designed using a bottom up approach in order to minimize the amount of excess space; this also minimized overall size and weight. With this in mind, the team placed each piece of instrumentation and then designed the fuselage around the placements. The POS had a problem with the center of gravity being to far back which caused the plane to be slightly unstable. To overcome this obstacle, the heaviest pieces of instrumentation—the fuel tank and the data logger—were placed as far forward as possible so the center of gravity remained in front of the neutral point. These items, having similar dimensions, were stacked in the first compartment of the fuselage, right behind the engine firewall. At this point, a support was placed.

To save additional space, the fuselage and wing teams worked together and decided to recess the wing box into the fuselage, as opposed to having it rest on top of the fuselage as was the case with the POS. After the first support was placed, the height of the fuselage was reduced

from 4.5 inches to 2 inches, allowing for wing box placement. The top of the wing box is flush with the original 4.5 inch height of the fuselage. Under the wing box, three compartments were created. The first compartment holds the receiver, pressure transducer as well as their respective batteries. The second compartment houses the servos for both the rudder and the elevator.

Supports were made in the third compartment under the wing box to allow the two carbon fiber rods from the tail to connect to the fuselage. The supports were plywood pieces with two circular cut-outs for the rods. All pieces of the fuselage were cut out using a LaserCamm. Figures 11 and 12 show the external and internal fuselage structures, respectfully.

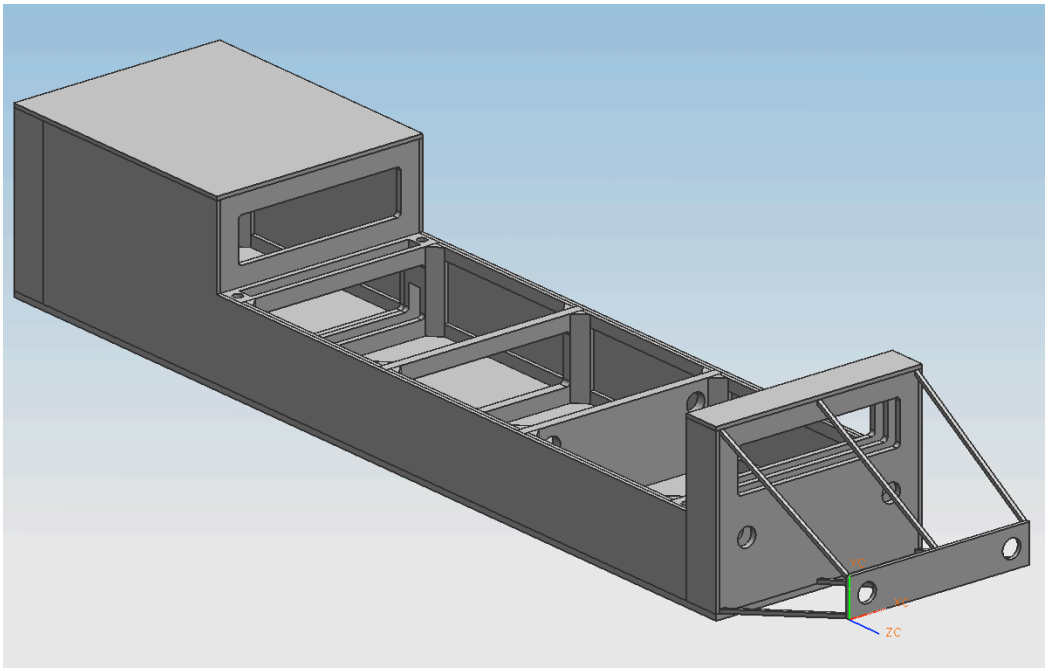

Figure 11. CAD Drawing of the Outside Structure of the Fuselage

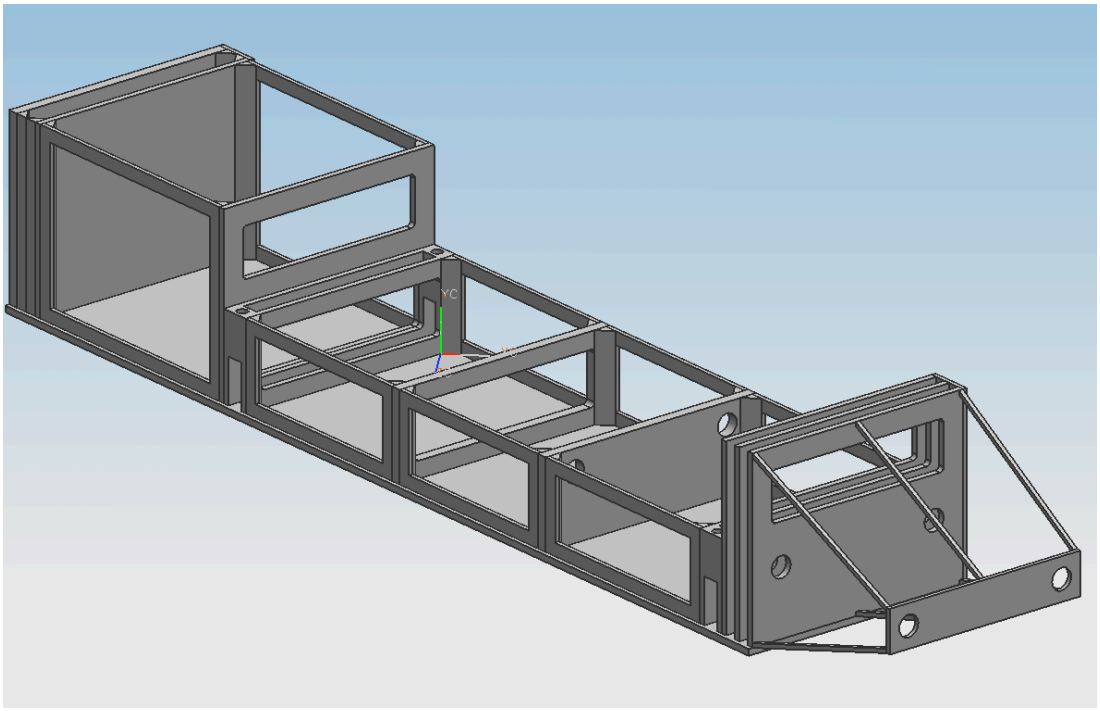

Figure 12. CAD Drawing of the Inside Structure of the Fuselage.

Other design aspects of the fuselage include detachable side panels so that the wing box does not need to be removed each time the instrumentation needs to be accessed. Also, above the fuel tank and data logger, a hinged plywood cover secured with magnets was added to the top for ease of maintenance. The fully constructed fuselage is presented in Figure 13.

To ensure that the carbon fiber rods connecting the fuselage to the tail were stable within the fuselage, a series of bulkheads were constructed. This design allowed for the rods to extend approximately thirty percent into the fuselage. During the flight and crash of the POS, the wing box sheared off from the fuselage. The new plane's design allows the bolts connecting the wingbox to the fuselage to extend through the fuselage. Two sheets of carbon fiber were placed on the bottom of the fuselage for structural reinforcement.

Figure 13. The fuselage, as seen from the front end, including the hinged plywood cover with magnetic closure.

The last section of the fuselage was built to be the main support for the tail. It has the same height and width as the front, boxed portion of the fuselage. Four supports were placed in this section to hold the booms in place. Three were housed inside this rear, boxed section and one was connected at the very end by balsa strips in order to give the plane a more aerodynamic shape as seen in Figure 14.

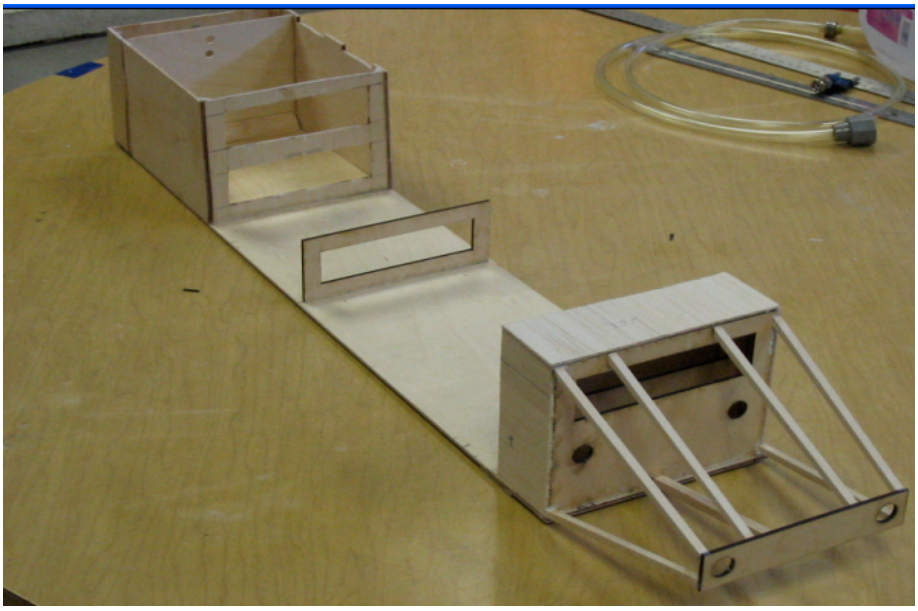

Figure 14. The back end of the fuselage showing the circular cut-out pieces of plywood for the carbon fiber rods to fit through.

No major problems were encountered during the construction of the fuselage. The most critical aspect in the construction process was to ensure that the carbon fiber rods of the tail would be able to slide into the supports. To allow for easy access to the components housed in the fuselage, removable sidewalls were built to cover the hollowed-out plywood frame. The original idea was to cover these sides with a layer of balsa wood—acting as an access panel to the inside of the fuselage—that would be attached with notebook bindings. These bindings would fit through a hole that went through both the balsa layer and the plywood at each end of the balsa panel. The problem with this idea was that the balsa is not strong enough to withstand the holes placed at each end; the very ends of the balsa wood were the only places where the balsa and inner plywood connected with each other and secured the removable panel closed. To resolve this issue, basswood was used instead of balsa wood for the panel and instead of the bindings, Velcro was used to secure the side panels shut. The Velcro works very well with the

basswood, as seen in Figure 15, as more durable than balsa and can withstand the force needed to peel the side panels from the Velcro.

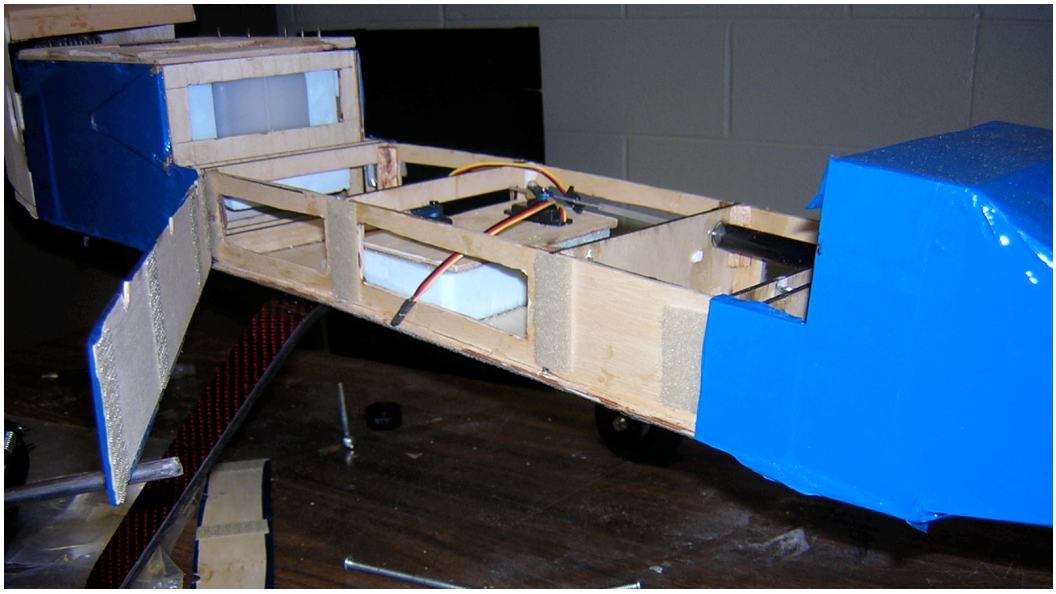

Figure 15. The removable fuselage side panels showing the Velcro connections.

Wings. This section is broken into three subsections. First, the design of the wings and wingbox is presented. Second, the process of fabricating the wings is discussed. Next, the surface finishing and implementation of wing control surfaces and morphing actuation systems is described.

Wing Design. The focus of this semester's design was creating a plane with a bottom up approach, built to meet the demands the team set. The backbone of the design was choosing wings that were functional and efficient. The first step the team took was researching airfoils that had been successfully incorporated in other Unmanned Arial Vehicles (UAVs) or R/C planes. Four airfoils were selected and analyzed using their individual lift coefficient vs. angle of attack curves. The plane also required an airfoil that would provide lift at zero angle of attack and be versatile enough to operate in both swept and unswept positions. Part of the selection

criteria was finding an airfoil that would be reasonable to model using CAD programs and fabricate. The team wanted an airfoil that would provide a high stall angle of attack with an impressive lift curve slope. The first option that was evaluated was the NACA 23015, an airfoil that has been used successfully in other R/C planes. The SD7304 Selig Donovan was the second airfoil considered. This is an experimental airfoil that has been shown to have high stall values and late separation properties. Third, the RXDBF014 was evaluated; this is an experimental airfoil that the Virginia Tech Design-Build-Fly Team considered during their 2003-2004 design process. The airfoil has an exceptionally high lift coefficient at zero angle of attack and shows stall values comparable to the other options. The NLF(1)-0115 is a new concept airfoil was created for UAV vehicles due to its laminar flow qualities and high lift curve slope. The lift coefficient vs. angle of attack graphs for each of these airfoils are shown in Figures 16 through 19. After discussion within the team, the NACA 23015 was chosen as the airfoil to be used on the plane.

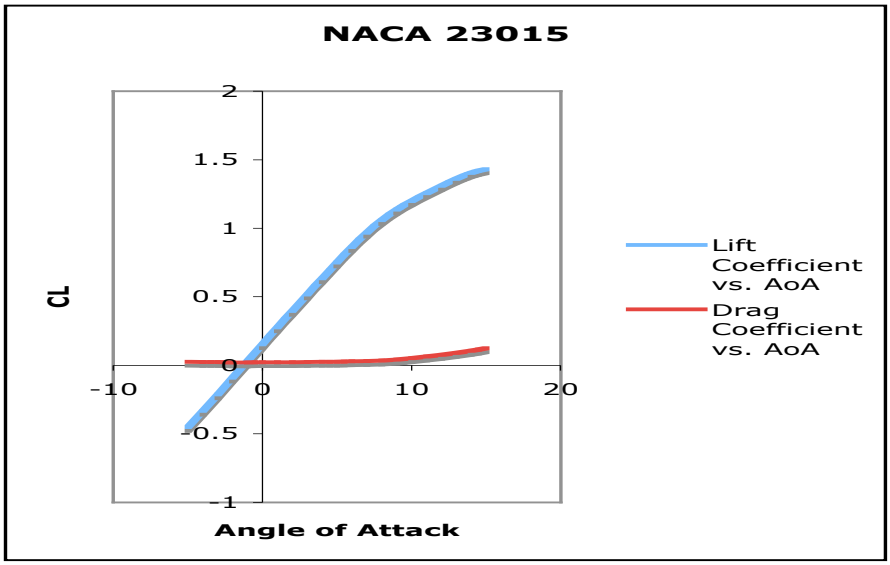

Figure 16. The NACA 23015 lift curve slope.

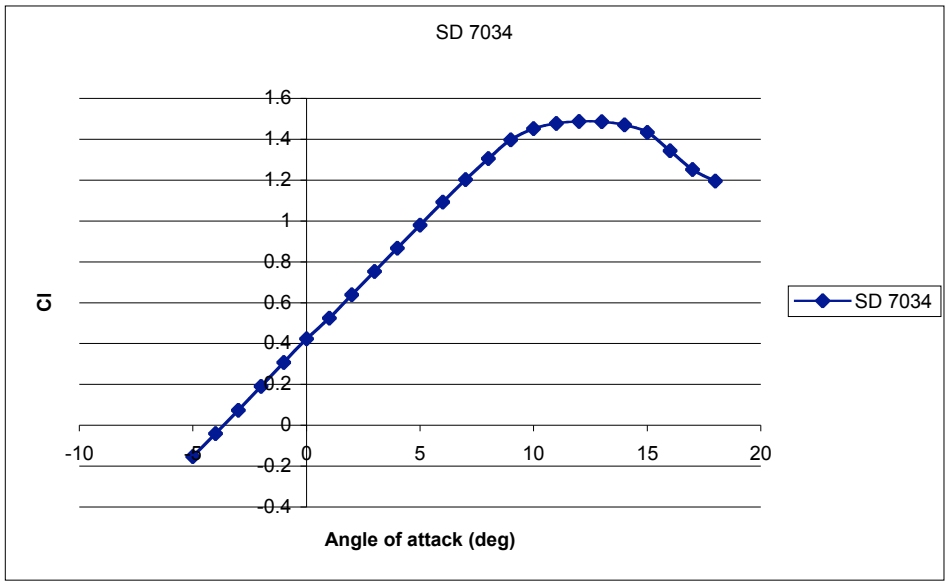

Figure 17. SD7034 lift curve slope.

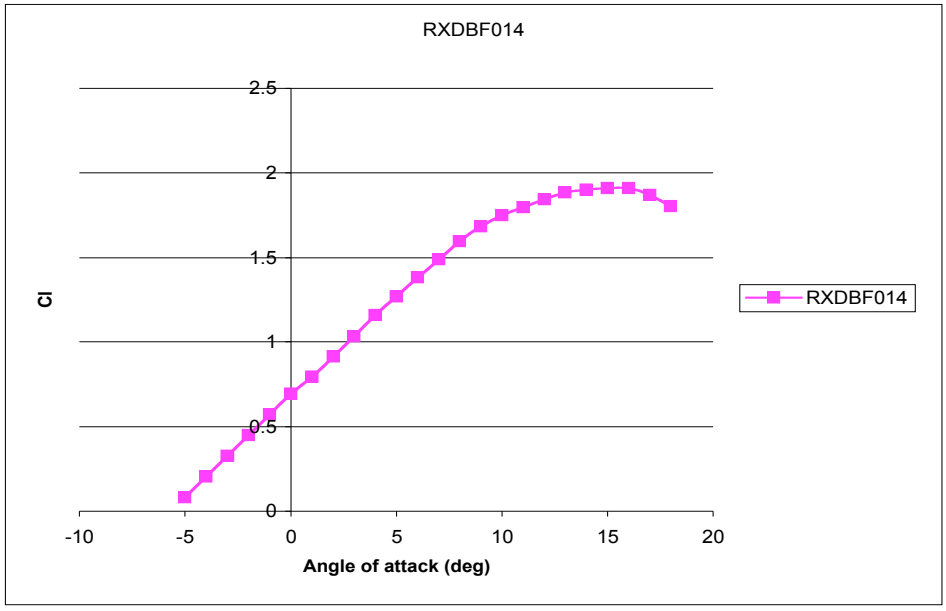

Figure 18. RXDBF014 lift curve slope.

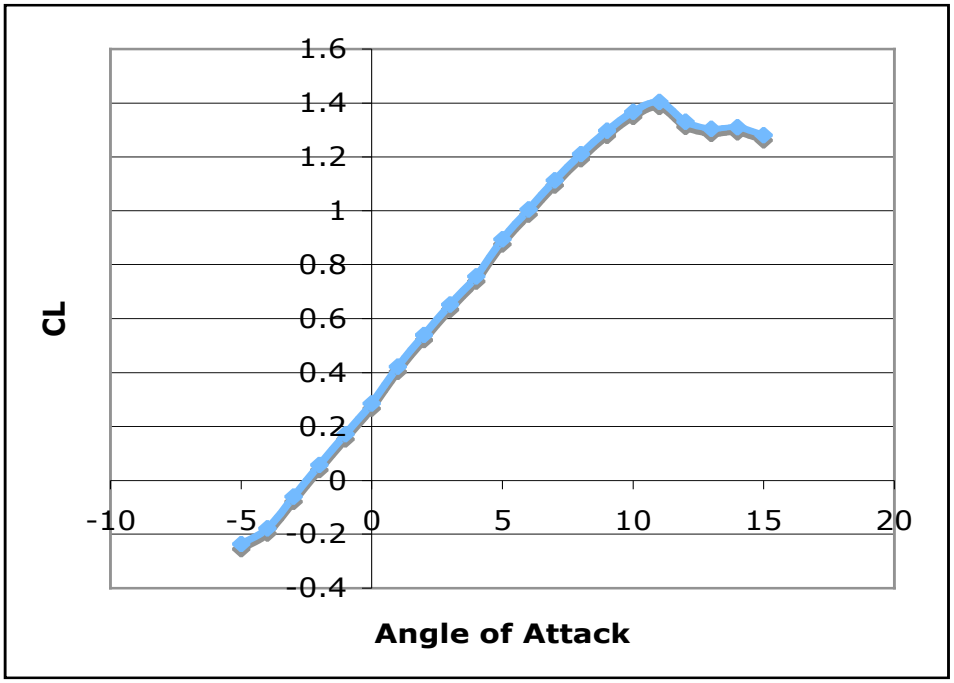

Figure 19. NLF(1)-0115 lift curve slope.

Witnessing the damage the wings on the POS suffered after the first crash, the team decided that use of more durable materials would be beneficial for the new plane. In the fall semester, a seminar was given by a professor from Brigham Young University who successfully incorporated the use of composite materials, including Kevlar and carbon fiber, in his UAV research designs. These materials proved to be both light and durable enough to sustain repeated crashes. After attending this presentation, we decided to explore the option of using advanced materials to create a more progressive wing design. Once the pros and cons for each of the available materials were considered, the wing team decided to move forward using carbon fiber.

The next step was choosing wing placement, initial sweep angle, and dihedral angle. For stability reasons and ease of construction, the team decided to place the wings halfway up the fuselage and to have an initial sweep angle of zero degrees. Dihedral angle was also set to zero

degrees due to the fact that the complexity of fabrication would not be balanced by the benefits it would provide.

The wing team realized that the bulk of the loads would be distributed within the wingbox. Therefore, reinforcing this portion of the plane was a prime concern. The use of plywood reinforced with carbon fiber worked out well in the POS so this concept was recycled for MWP-06. The wingbox was designed for the wings to be sandwiched between two layers of the reinforced plywood while also allowing for 45 degrees of sweep with space between the wings to allow for actuation components.

The goal of this semester's design was to create a lighter and smaller plane that would be easier to fly. As a part of this effort, we adjusted weights in order to keep our wing span under six feet. Using Raymer's Aircraft Design book, the team set the wingspan at five feet. Ailerons were designed to have a length of ten inches with a chord of two inches. Analyzing the benefits of extension length vs. performance, the length of each wing extension was set to one foot, ten inches of which would extend from the wing during actuation. The extension airfoil would incorporate the same NACA 23015 airfoil as the wing, scaled down to fit snugly within the main outer frame.

Wing main body fabrication. The first component of the wings was a foam core cut into the shape of a NACA 23015 airfoil. This core served two purposes; first, as a mold for the carbon fiber fabric, and second, as a matrix to mount morphing actuation within. It was the initial intent of the wing team to complete all necessary work on the plane wings within the CIMSS lab. Outsourcing, aside from being extremely overpriced, was viewed more as a concession to a challenging situation than a necessity. However, after several weeks of attempts at shaping the foam core with the materials available in the lab, it was concluded that the

accuracy needed for the cuts could not be achieved without help from an outside source. To aid in the construction, RADVA, a leading manufacturer of custom foam shapes, was hired to cut the foam core.

The core for each wing consisted of two sections. The first section was solid with a 45 degree cut from mid-chord to trailing edge removed allowing the wings to sweep back without contacting each other. Three holes running the length of the core were included to house both the carbon fiber tracks the wing extensions would slide on and a guide for the rack used for extension actuation. The second section was hollowed out to house the wing extensions. Once cut, the two cores were glued together on either side of the wing's one internal rib. The finished product can be seen in Figure 20, the solid core to the right of the wooden rib, the hollowed section to the left.

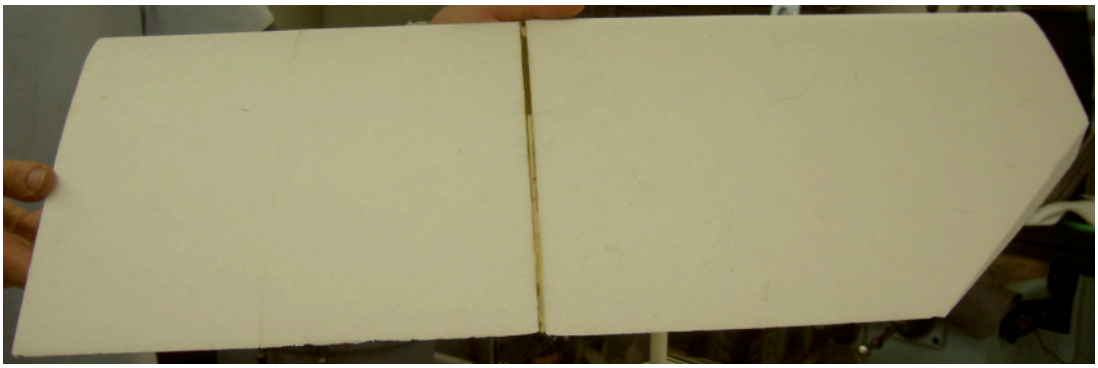

Figure 20. Completed solid foam core section glued together and ready for an outer composite layer.

Laying the carbon fiber over the foam core was the next step in wing fabrication. It was decided in advance that two layers of carbon fiber as an outer skin would be sufficient for even the strongest loading the plane wings would experience during flight. In addition to these, a layer of unidirectional fabric was added to the bottom of both wings in order to resist any flexing in the wing caused by lift.

To begin, the two layers of carbon fiber for each wing were cut out, leaving several additional inches on each edge to assure a full overlapping surface. The first of these layers can be seen in Figure 21. With these layers cut to size, a mock wrap up of the wing was completed in order to add additional cuts on the carbon fiber, allowing it to be smoothed evenly around each edge of the wing once epoxy had been applied.

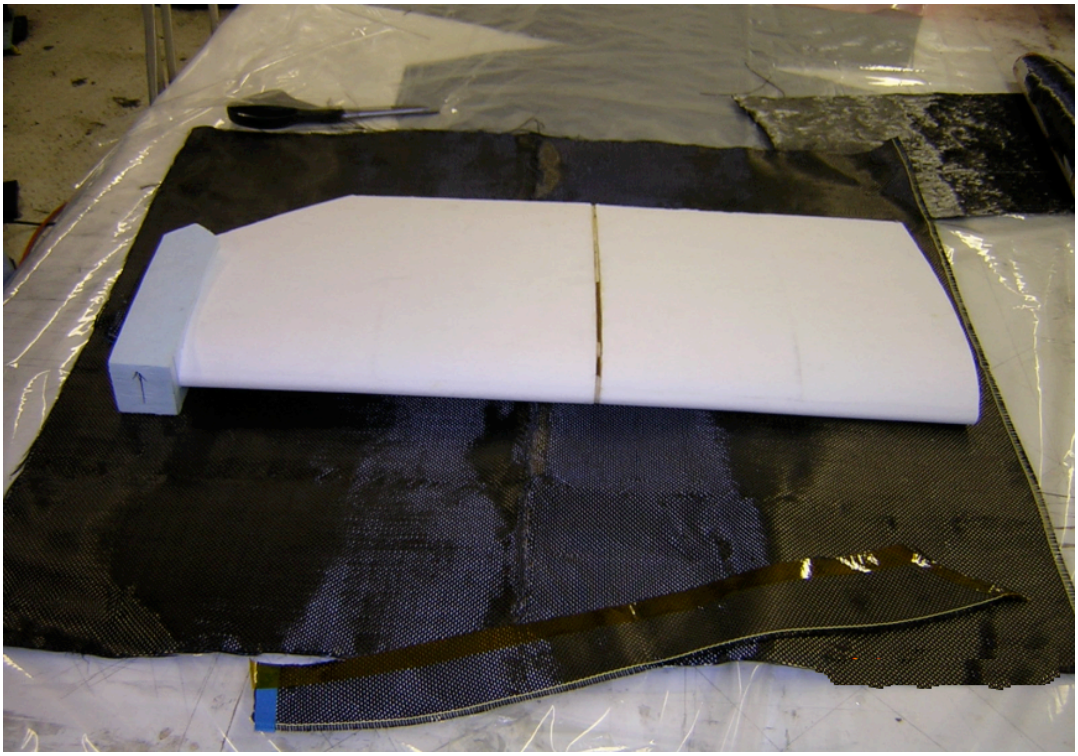

Figure 21. First step in laying carbon fiber: Cutting sheets for the main skin, assuring a fully covered homogeneous surface once covered with epoxy resin.

Additional strips of reinforcement were included at the wing root and at the rib seam, mid-wing. One strip can be seen already cut at the bottom of Figure 21. Having completed the cutting for these layers, the unidirectional fabric for the underside of the wing was cut to size.

With all pieces sized, a bowl of West Systems Epoxy was mixed and then generously applied to the first sheet of carbon fiber. Once saturated, the wing was wrapped with the wetted

sheet. To attain the smooth surface, scrapers were used to remove any wrinkles or bumps in the fabric. The scrapers also helped remove excess resin thereby helping to reduce the overall weight of the wings. This epoxy application and smoothing process can be seen in Figures 22 and 23. Once the first layer of fabric had been smoothed applied and smoothed over the core, the wing was flipped over and the layer of unidirectional fabric was applied as shown in Figure 24.

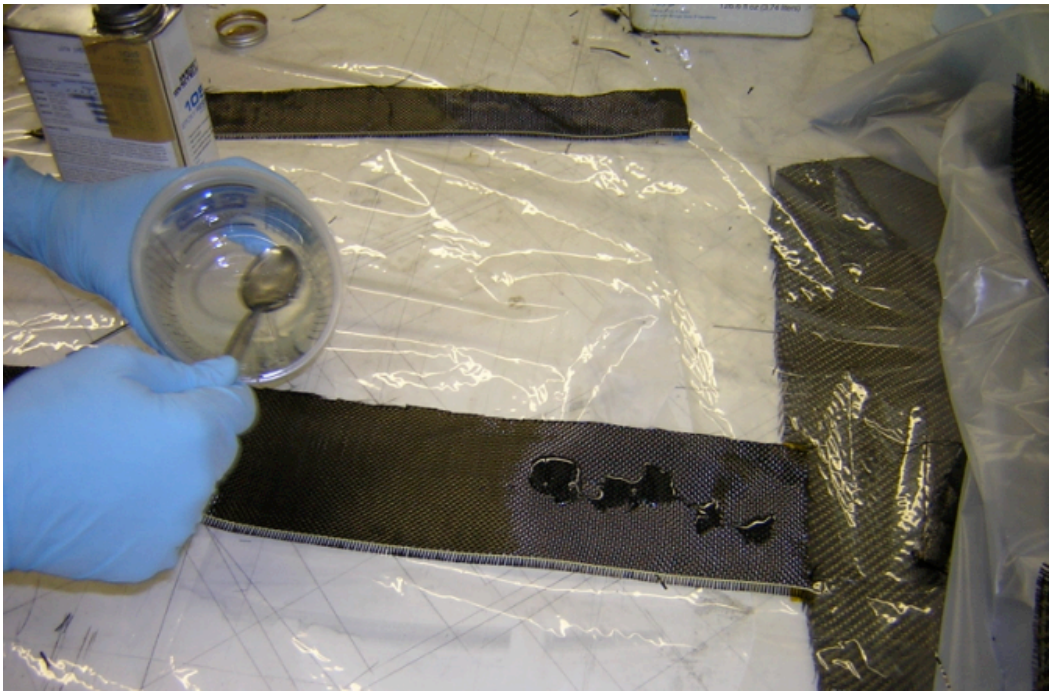

Figure 22. Second step in laying carbon fiber: Applying epoxy to the carbon sheeting, assuring a fully wetted surface.

Figure 23. Third step in laying carbon fiber: Smoothing of the wetted fiber over the foam core and removal of excess epoxy using scrapers.

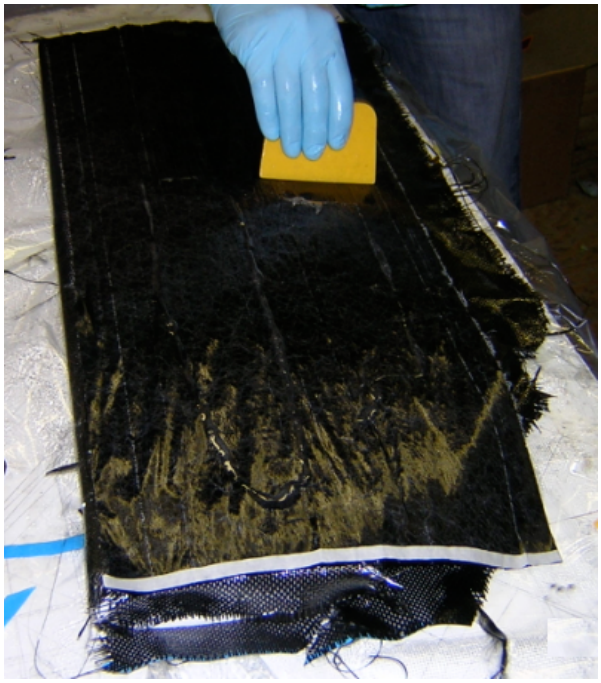

Figure 24. Third step in laying carbon fiber: Application of the unidirectional carbon fiber fabric to the underside of the wing.

After applying the reinforcement to the wing underside, the final layer of carbon fiber was applied and smoothed, as presented in Figure 23. In addition to the standard smoothing needed to achieve a flat wing surface, more manipulation of the carbon fiber around the wing end caps was required. The end caps were an addition to the wing allowing the wings to pivot upon a flat surface. However, the high pressures involved with the vacuum bagging caused significant deformation of the end-caps, eventually leading the team to replace them with thin plywood surfaces instead.

With all layers of fiber applied to the wing, the actual process of vacuum bagging began. First, the wings were wrapped in peel ply, a fabric impregnated with a release agent to keep it and additional layers in the bagging process from sticking to the fiber. Next, a thin sheet of perforated release film was wrapped around the wings. This film was also treated to minimize any bonding between it and the peel ply underneath. The perforations consisted of thousands of holes which allowed the pulling of epoxy through its surface and into the next absorbent layer. The final layer encasing the wings before the actual vacuum bag was the bleeder, a thick sheet of fluffy cloth which acted as sponge to soak up all excess epoxy from the wing surface. Once sealed within the bag, the bleeder also prevents wrinkles caused by air evacuation from creating air pockets and blocking the air path for pulling the vacuum. Now fully covered, the wing was inserted into the bag, a durable sheet of plastic folded in half and sealed along each edge with bag sealant tape. The tape, once acted on by the vacuum pressure, creates a leak proof seam allowing maximum vacuum within the bag. The wing, wrapped in the final layer of bleeder fabric, can be seen within the vacuum bag in Figure 25. The yellow sealant tape is also visible along each edge of the vacuum bag.

Figure 25. Final step in laying carbon fiber: Once wrapped in peel ply, release film and bleeder, the wing was inserted into a large vacuum bag, sealed on all edges by bag sealant tape (BST).

Once inside the bag, two tube leads from the vacuum pump were inserted on opposite sides of the bag, and the vacuum was turned on. Within seconds, the air was completely removed, and a bag was sucked tightly against the wing. Pump insertion points and the fully evacuated bag are shown in Figure 26, followed by a picture of the finished product, ready for sanding and the addition of ailerons and extensions, in Figure 27.

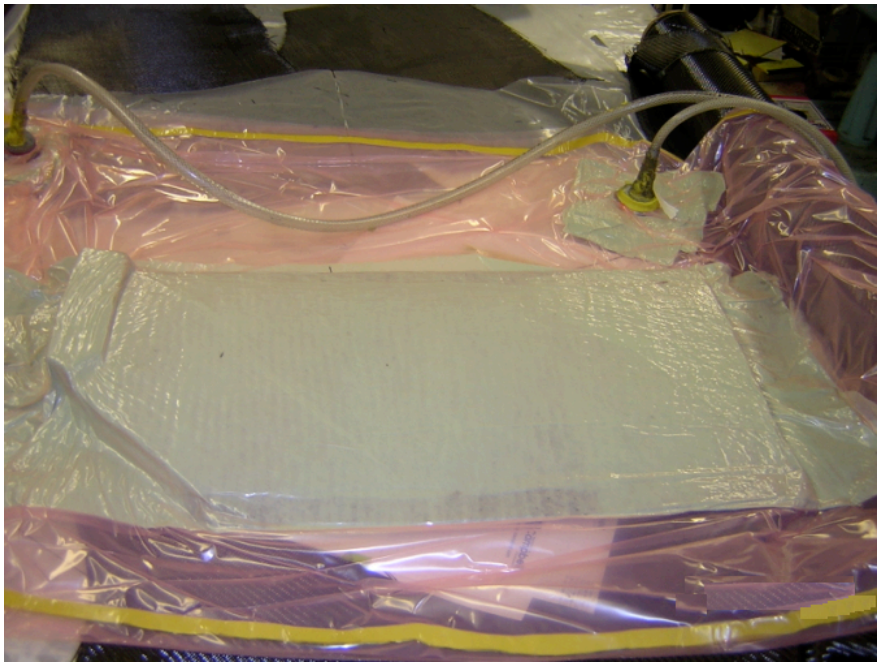

Figure 26. The fully evacuated vacuum bag, under pressure for twenty-four hours.

Figure 27. A carbon fiber covered wing ready for finishing.

Wing Finishing Tasks. In addition to the previously mentioned deformation of the end caps due to the high pressures experienced during the vacuum bagging process, the wings were also deformed in several locations. The team used microballoon fillers followed by a wet sanding process in an effort to attain aerodynamic wing surfaces.

Next, the ten inch by two inch sections to be used for the ailerons were cut from the trailing edge of each wing. The ailerons were mounted using duct tape hinges glued between wooden blocks in both the wing and the aileron, presented in Figure 28. This method allows the ailerons to move rigidly and evenly while maintaining a connection that is flexible and will retain strength after many actuations.

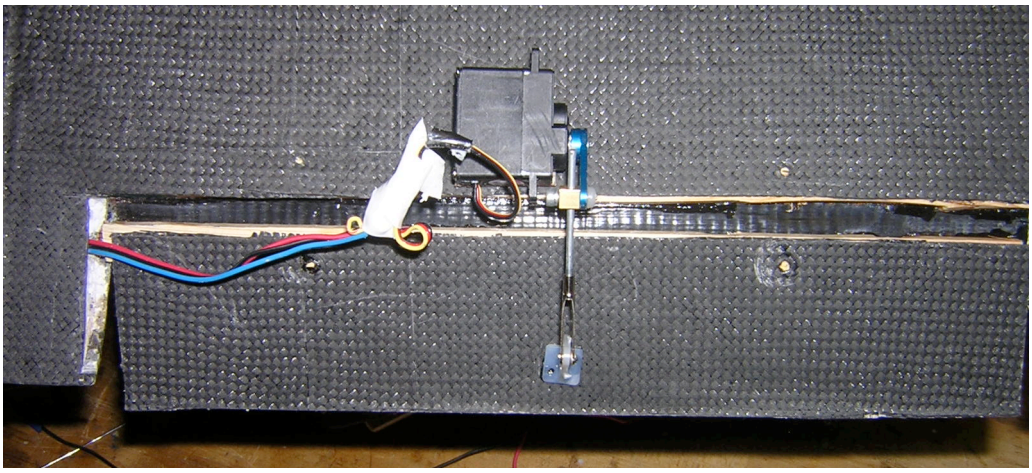

Figure 28. Aileron attachment including tape hinge and servo placement.

In order to achieve wing sweep under loaded conditions, the team designed a rotation point at the location where the wings attach to the wingbox. The first step was to carefully align the wings within the wingbox to ensure that they would evenly sweep and that they would provide the five foot wingspan specified by our design criteria. Next, holes were drilled simultaneously through the wings and both layers of the wingbox. The holes inside the wings were hollowed out to allow for the placement of an aluminum tube to be used as a bearing

housing. This assembly, pictured in Figure 29, allows for wing sweep with minimal friction despite wing loading.

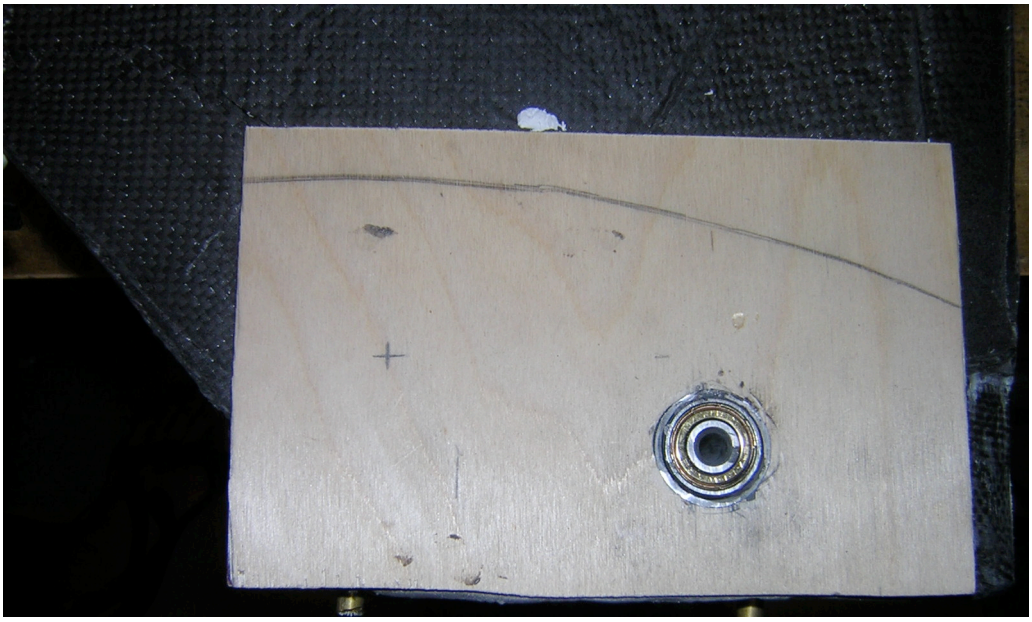

Figure 29. Rotation point between the wings and the wingbox.

Morphing Actuation

This subsection presents the two morphing capabilities designed into MWP-06 and the methods used to actuate.

Wing Extension. After discussing many options, the wing team decided to utilize a rack and pinion system to achieve span extension. Two racks and two pinions were necessary to achieve this morphing effect. The entire system was originally designed to operate using two Speed 400 Motors. However, after the wings were fully assembled, the team discovered that the motors did not provide enough torque to overcome the friction between the wing extension and the extension cavity. To solve this issue, two HS85MG servos were modified; the PWM signal wires were cut so only the connections feeding directly to the motor inside the servo box were utilized. To limit the span extension, two kill switches, a Super Rooster Reversible Speed Controller, and a battery were connected to one of these motors. To ensure symmetric operation

of both wing extensions, the second motor was connected in parallel to the first. Since the two motors must operate in opposite directions at all times, the positive connection on the first was connected to the negative on the second and the negative connection on the first was connected to the positive on the second. A diagram depicting this circuitry is presented in Figure 30. The rack and pinion system outside of the wing is shown in Figure 31. Figure 32 shows the mounting of the rack and pinion servos in a wing.

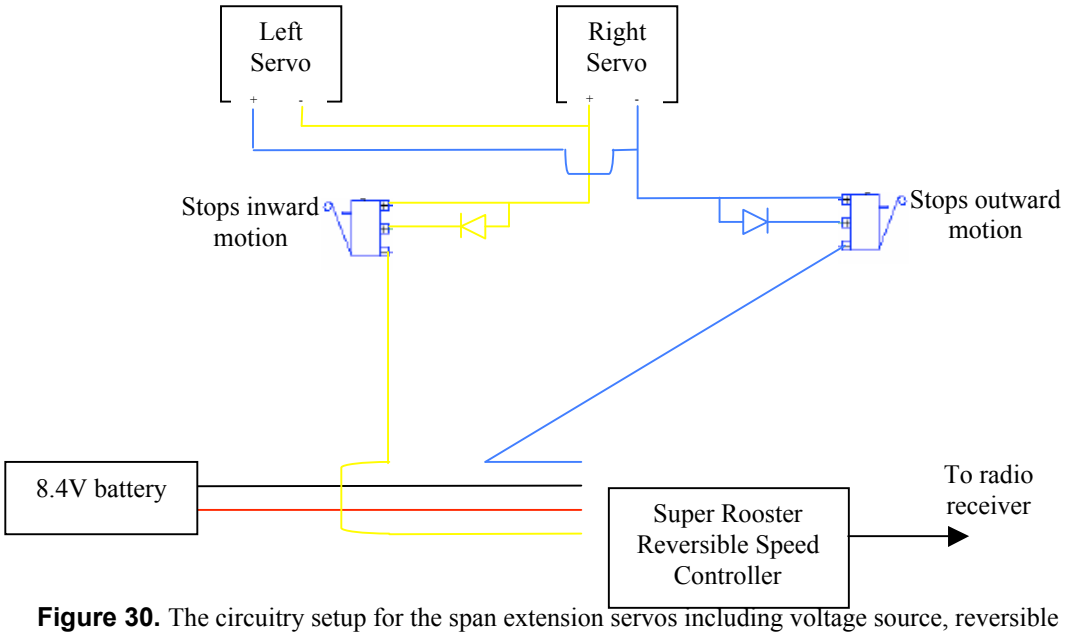

Figure 30. The circuitry setup for the span extension servos including voltage source, reversible speed controller, and kill switches.

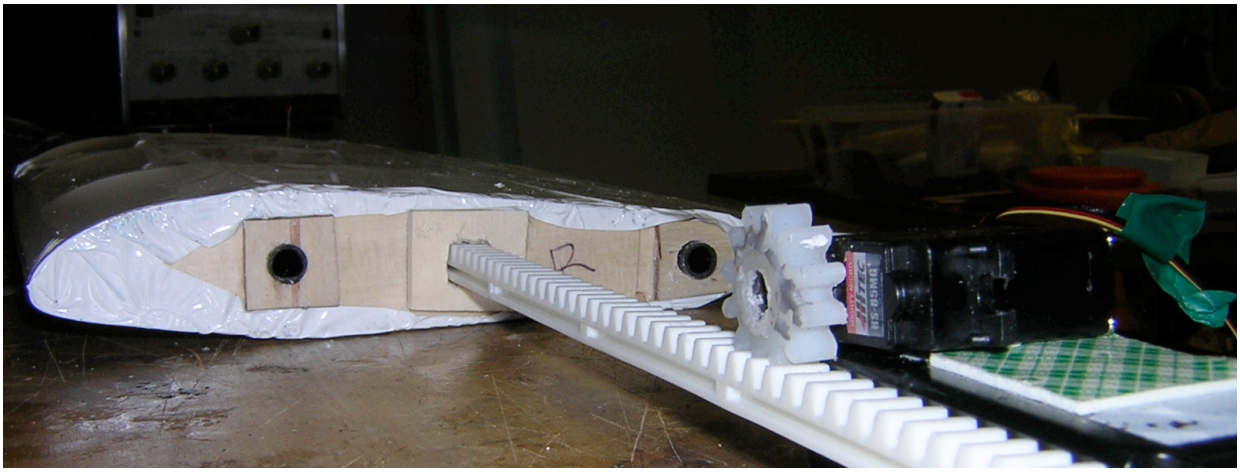

Figure 31. The rack and pinion system used in the actuation of the span extensions.

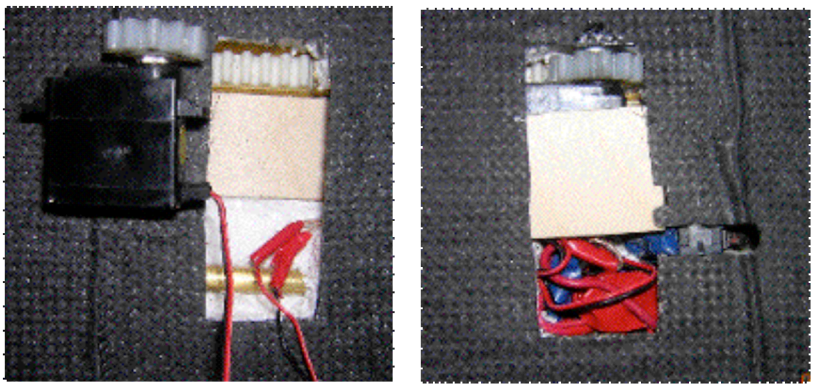

Figure 32. The internally mounted rack and pinion servos.

Wing Sweep. The design and application of the sweep actuation was a semester long ordeal involving four design options, each of which was viable, with only one being truly effective and feasible. With two weeks remaining before the scheduled plane completion deadline, the decision was made to place a HS-805BB high torque servo combined with a matching gear box above each wing's pinned connection point. By rigidly securing the gears to each wing, nearly 1300 ounce-inches of rotational torque could be applied to obtain a symmetric wing sweep of 45 degrees. This torque figure surpassed the worst case scenario of a 2.5 pound drag force acting at the wing tips, thereby allowing wing sweep under any potential loading condition. Furthermore, based a force feedback controller within the potentiometer, the wings will remain swept by resisting any rotational moment caused by drag forces with an equal and opposite moment.

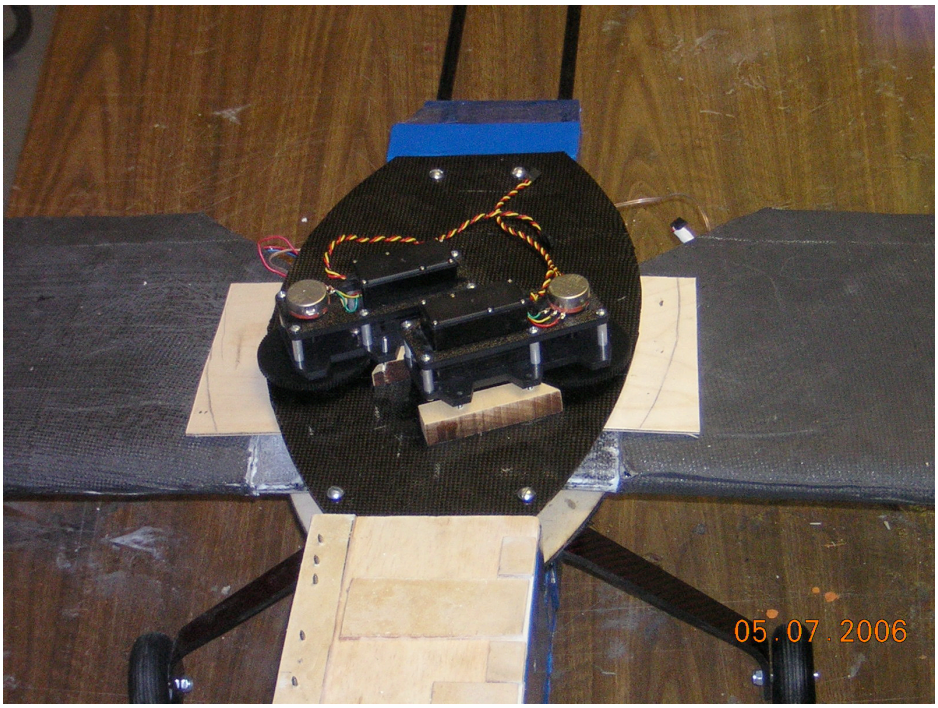

Figure 33. The sweep actuation setup, including the servos and gear boxes.

Power Draw Constraints. To ensure that actuation of all control surfaces would be possible throughout the duration of a flight, it was necessary to determine the operational time for each of the batteries being used. To do this, the team compared the power draw of each motor with the capacity of the corresponding battery to determine which battery is the limiting factor.

The current plane utilizes three Nickel-Cadmium batteries to power all of its actuation systems. The battery that powers the sweep is rated at 8.4 V and 1400 mA-hr, providing a capacity of 11.76 W-hr. A second 8.4 V battery rated at 600 mA-hr provides the power necessary to control the span extension. This battery has a capacity of 5.04W-hr. The receiver battery is rated at 6.0 V and 1700 mA-hr, which provides a capacity of 10.2 W-hr. This battery is responsible for powering the motion of all of the control surfaces, the throttle, and the landing gear (which moves with the rudder). In order to determine the operating time for each battery, it

was necessary to determine the current draw associated with each motion during both idle and working times. The current draw values were provided by the manufacturers. Our team conservatively estimated the percentage of working time for each control surface motion. Table 4 shows a summary of all of the important elements in this analysis. Figure 34 shows a schematic of the servo, battery, and receiver connections.

Table 4. Parameters used in power draw analysis.

Motion	**Battery**	**Servo**	**Current Draw (A)**		**Frequency of Use (% of flight time)**	
			Idle	**Working**	**Idle**	**Working**
Sweep	8.4 V	HS 5995 TG	0.38	5.2	90	10
Span extension	8.4 V	HS 85 MG	0.0086	0.26	90	10
Elevator	6.0 V	HS 81 MG	0.0091	0.280	50	50
Rudder	6.0 V	HS 81	0.0091	0.280	85	15
Landing Gear	6.0 V	HS 81	0.0091	0.280	85	15
Ailerons	6.0 V	HS 81 MG	0.0091	0.280	50	50
Throttle	6.0 V	HS 81	0.0091	0.280	90	10

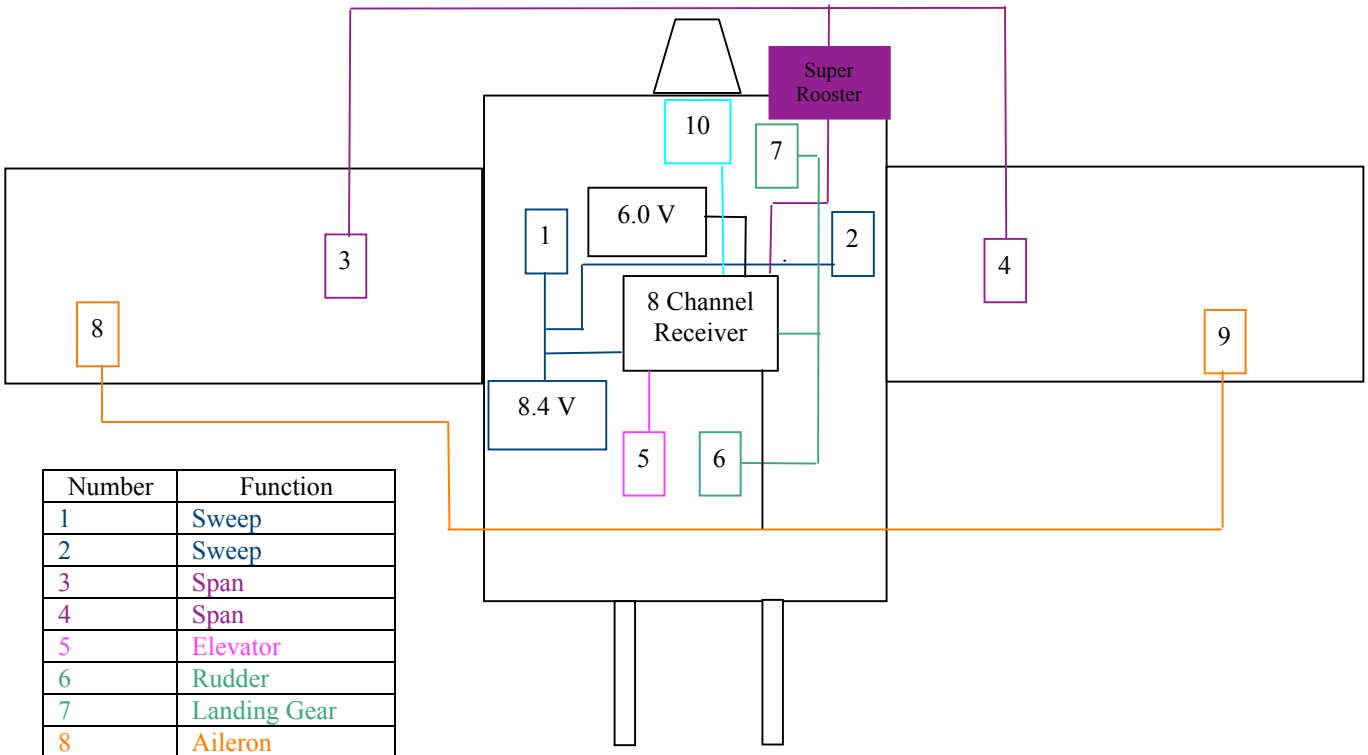

Number	Function
1	Sweep
2	Sweep
3	Span
4	Span
5	Elevator
6	Rudder
7	Landing Gear
8	Aileron
9	Aileron
10	Throttle

Figure 34. Schematic of actuation connections.

To find the power draw, we used Ohm's Law, which gives the basic relationship between current, voltage, and power. For each motion, the power draw during idle times (P_{idle}) and the power draw during working times ($P_{working}$) were calculated. By using the estimated percentages of working time and idle time for each motion, we were able to find the continuous power draw using equation 3:

$$P_{continuous} = \%_{idle} * P_{idle} + \%_{working} * P_{working} \qquad (3)$$

The estimated operating time for each battery, *t*, was found based on the capacity of the battery (in W-h) and the total continuous power draw (in W) from that battery, as shown in equation 4:

$$t = \frac{C_{battery}}{P_{continuous,total}} \tag{4}$$

where $C_{battery}$ is the capacity of each battery. The results of this analysis are shown in Table 5. The flight time is limited by the 8.4 V battery powering sweep; it has an operation time of about 48 minutes based on the team's conservative assumptions.

Table 5. Results of power draw analysis.

Battery	Operating Time
8.4 V 1400 mAh NiCAD	48 minutes
6.0 V 1700 mAh NiCAD	2 hours, 40 minutes
8.4 V 600 mAh NiCAD	8 hours, 53 minutes

Finances

The team expenditures during the Spring 2006 semester are presented in Table 6. As shown, the total amount spent during this semester is $2635.65. This includes costs for repairing the POS as well as all design and construction costs associated with MWP-06. Our largest expenditures were on wind tunnel use, servos, and composite materials. Table 6 also lists the total amount spent during the fall semester. The grand total of expenditures of the 2005-2006 Morphing Wing Team is $3615.01, which is well within the team's original budget of $5000.

Table 6. Breakdown of expenditures of the Morphing Wing Team during the Spring 2006 semester.

Date	Company	Item(s)	Total Price
1/24/06	Barnes & Noble	Model Aircraft Books	$74.88
1/26/06	Aerospace Composites	Epoxy Supplies	$150.50
1/26/06	McMaster-Carr	Threaded rod, etc.	$40.69
1/26/06	Tower Hobbies	Blue Monokote	$29.97
2/1/06	Heavener's	Craft Hand Drill	$17.49
2/4/06	Target	Scales	$69.26
2/10/06	Servo City	Servos	$322.56
2/10/06	Tower Hobbies	Deluxe Heat Gun	$32.98
2/10/06	AOE Wind Tunnel		$604.00
2/21/06	Heavener's	Stock Drive Products	$25.69
2/24/06	Hobby-Lobby	7.2 V Motors	$20.30
2/27/06	The Composites Store	Carbon Rods	$110.02
3/3/06	Jamestown Distributors	Epoxy Resin/Hardener	$70.40
3/3/06	Servo City	Batteries, Speed Controller	$75.70
3/10/06	CST Sales, Play It Again Sports, Reeds Lumber	Composites, Bearings, Foam	$210.90
3/13/06	Jo-Ann Fabrics	Pins	$5.23
3/13/06	Lowe's	Paneling	$18.15
3/13/06	Mish-Mish	Balsa	$28.44
3/14/06	Mish-Mish	Plywood	$21.52
3/15/06	Mish-Mish	Plywood, Balsa, Fasteners	$54.30
3/17/06	Home Depot	Drill Bit	$10.29
3/19/06	Lowe's	Drill Bit	$7.32
3/19/06	Mish-Mish	Balsa, etc.	$4.16
3/20/06	Mish-Mish	Plywood, Bass Wood	$21.36
3/20/06	Mish-Mish	Super Glue	$3.44
3/21/06	Mish-Mish	Plywood, Bass Wood	$16.23
3/24/06	Mish-Mish	Plywood	$21.52
3/26/06	Mish-Mish	Plywood, Balsa	$17.38
3/27/06	Mish-Mish	Adhesive, Bass Wood	$12.55
3/28/06	Mish-Mish	Sharpie, Bass Wood	$4.58
3/31/06	Mish-Mish	Return Credit	-$5.87
4/21/06	Crossroads Hobby	Brass Tubing	$15.50
4/21/06	Reed's, Lowe's, Advance	Foam, Fasteners, Belt	$71.38
4/26/06	Servo City	Batteries	$77.90
4/28/06	Heavener's	Nuts, Bolts, K&S, Velcro, Tape	$26.09
5/2/06	Servo City	Gear Boxes	$117.29
5/4/06	Servo City	Servos, Gear Boxes	$231.55
	Total, Spring 2006		$2,635.65
	Total, Fall 2005		$979.36
	Grand Total		**$3,615.01**

Analysis of MWP-06

This section presents the different analyses done on MWP-06. These include summaries of the structural analysis on the wing box completed with ANSYS, the theoretical analysis performed in Tornado that was confirmed with VLMpc, the results achieved with USAF DATCOM, and the mass balance performed to calculate the location of the center of gravity.

Finite Element Analysis on the Wing Box

To investigate the structural integrity of MWP-06, the team used finite element analysis tools. The analysis was performed on the wing box. This structure was chosen based on the fact that it will see the highest stress concentrations. The wing box, constructed with carbon fiber and epoxy, was analyzed using a program called P.E. Structures. The material properties used in this program are presented in Table 7.

Table 7. Material Properties

Density	1.57 g/cc
Young's Modulus	190 Gpa
Poissons ratio	0.49
Yield Strength	200 Mpa
Ultimate Strangth	810 Mpa
Thermal Expansion coefficient	1.5/ºC

The wing box structure, which attaches the wings to the fuselage of the plane, was analyzed with P.E. Structures. The wing box is attached to the fuselage with four bolts, one at each corner. The wings are connected by the bearing system previously described. In order to model the behavior of the wing box, the four corner holes were constrained in all degrees of freedom—both translational and rotational. The load was applied to the contact area between the bearing system and wing box. A smart meshing feature in P.E. structures was chosen to

determine the element size. Tetrahedral elements were used in this analysis. The meshed and loaded structure can be seen in Figure 35.

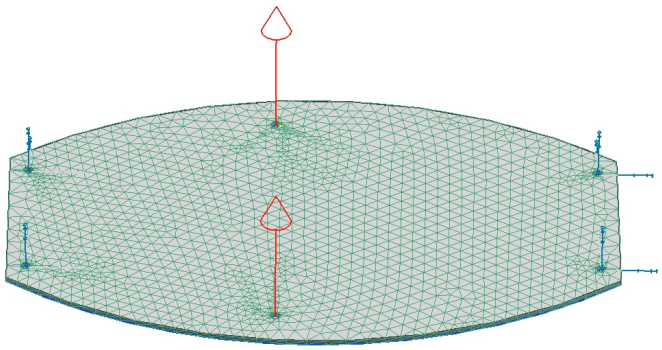

Figure 35. A FEA model of the wing box.

The analysis was first run with two 15 lb_f loads applied to the bearing connections. This loading represents a 1G test. The von Mises stress seen in the structure under these loading conditions can be seen in Figure 36.

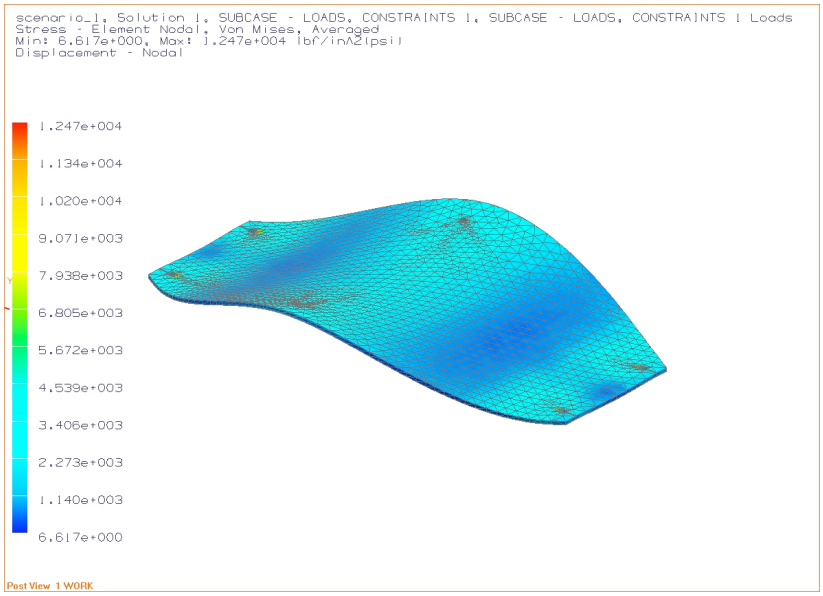

Figure 36. Wing Box under 15 pound load

The highest stress seen by the wing box is 12,470 psi, which is equivalent to 86 MPa. This stress is well under the yield strength of the material. It was desired to determine the load on the bearing system that would lead to a failure of the structure. To find this failure point, the analysis was run several times, increasing the loads by 15 lb_f per run. The maximum von Mises equivalent stresses that the wing box experienced was then compared to the ultimate strength of 810 MPa. Using this method, we determined the structure will fail under a 150 lb load—equivalent to 10G's. Figure 37 plots the displacement of the deformed wing box. The maximum displacement is 0.02 inches before failure. Figures 38 and 39 present the stress distribution in the wing box under the 10G loading. The stress seen under the 10G loading is 859 MPa. This stress occurs at the four locations where the wing box is bolted to the fuselage.

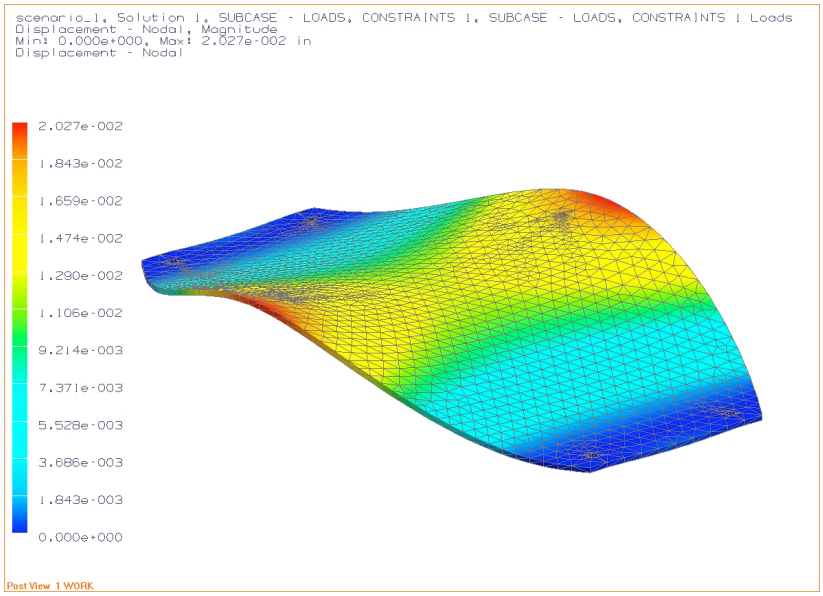

Figure 17. Deformed Wing Box.

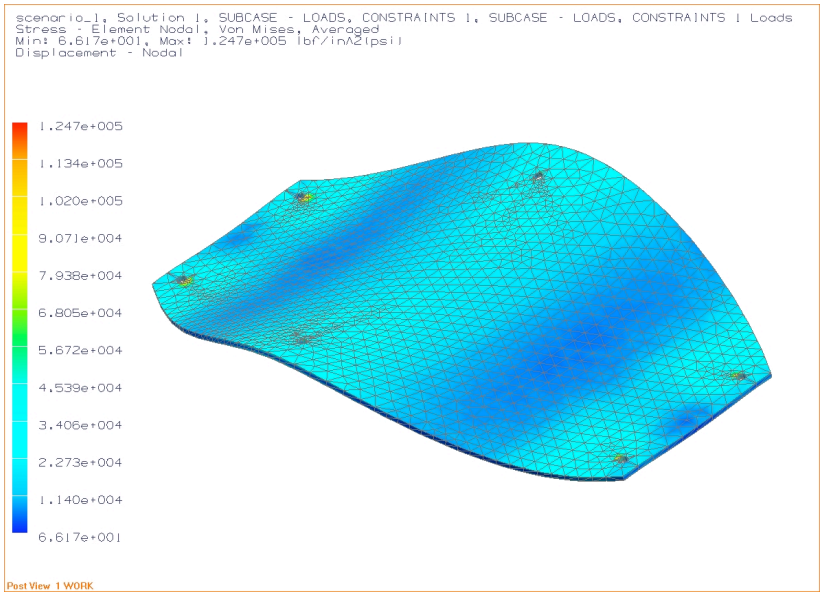

Figure 38. The von Mises stress from 10G loading

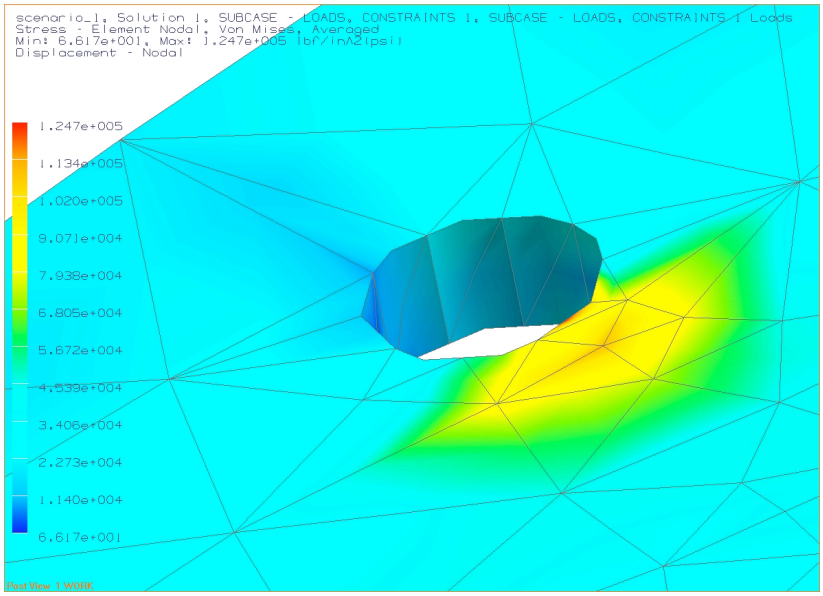

Figure 39. Zoomed in view (corner bolt) of von Mises stress under 10G loading

Theoretical Analysis

Vortex Lattice Method Analysis Using VLMpc. A vortex lattice method (VLMpc) was used to analyze the center of gravity (CG) shift along with the neutral point (NP) shift with changing sweep degrees of the wings with and without span extensions. The analysis will also compare the lift curve slope of both wings with and without span extension. This two surface

vortex lattice method was developed at NASA Langley by John Lamar. The vortex flows are estimated by the leading edge suction analogy and uses a limit of 200 panels to represent the two lifting surfaces. The plane has a wing span of 5 feet without span extensions, a horizontal tail span of 1.29 feet, and an overall length of 6 feet. A detailed plot of the wing/tail geometry without span extensions used in the vortex lattice method program is presented in Figure 40.

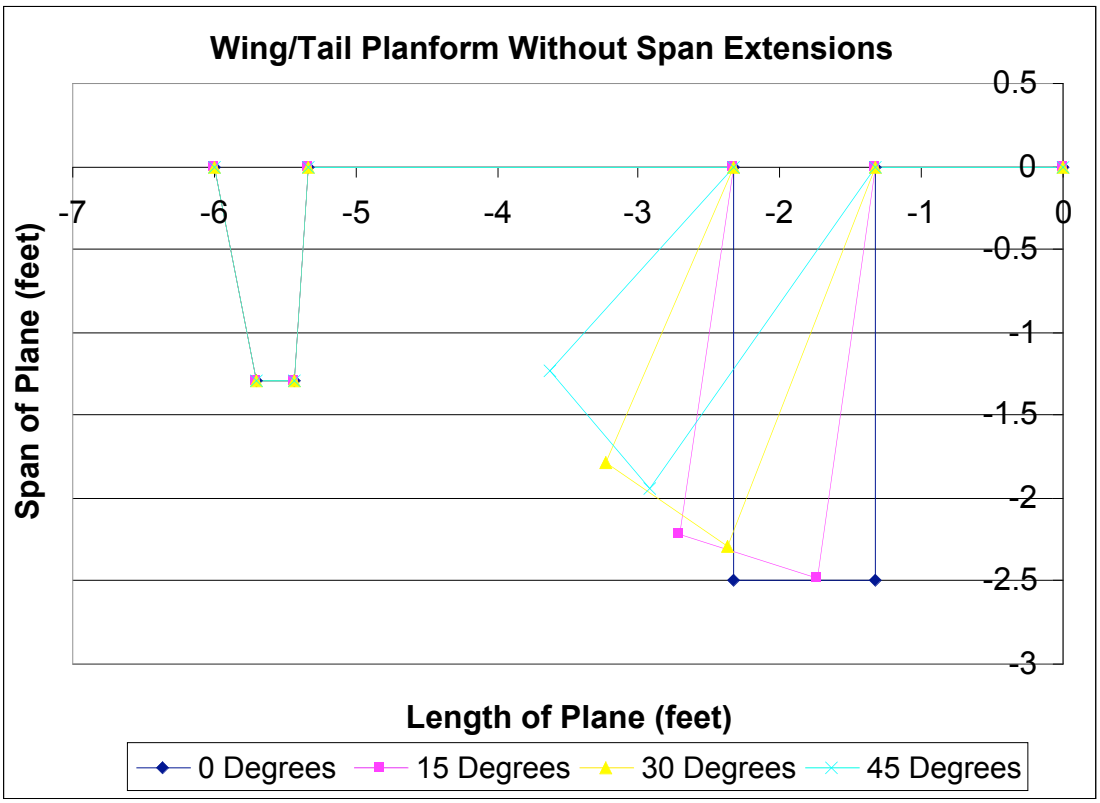

Figure 40. A detailed plot of wing/tail geometry at different sweep angles without span extensions.

VLMpc is capable of generating data simply by recording the coordinates of the planform as shown above, the number of spanwise and chordwise panels, and the Mach number. The number of spanwise panels used in the program was sixteen; eight chordwise panels were applied for all sweeps. A Mach number of approximately 0.03 was used in the program. The two major sets of data that VLMpc calculates are the neutral point position and the lift slop curve. The center of gravity was then calculated to be 10% MAC stable. Tables 8 and 9 along

with Figures 41 and 42 show the relationships between center of gravity, neutral point, and lift curve slope to angles of sweep without span extensions.

Table 8. Neutral point and center of gravity as a function of wing sweep angle without span extensions

Neutral Point			Center of Gravity	
Sweep (deg)	NP (feet)		Sweep (deg)	CG (feet)
0	2.05383		0	1.95383
15	2.23453		15	2.13453
30	2.54715		30	2.44715
45	2.85686		45	2.75686

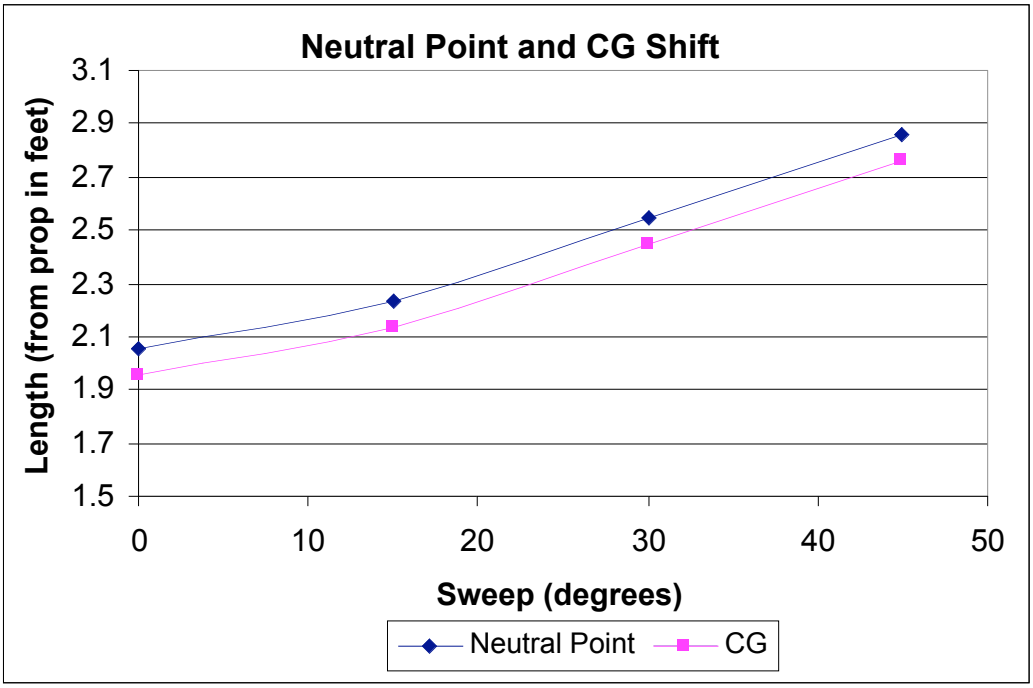

Figure 41. Plot of neutral point and center of gravity shift with wing sweep angle without span extensions. Noting the center of gravity is 10% MAC stable.

Table 9. Lift curve slope as a function of wing sweep angle without span extensions

Lift Slope	
Sweep (deg)	Lift Slope (Cl per radians)
0	4.62493
15	4.46364
30	3.92959
45	3.03551

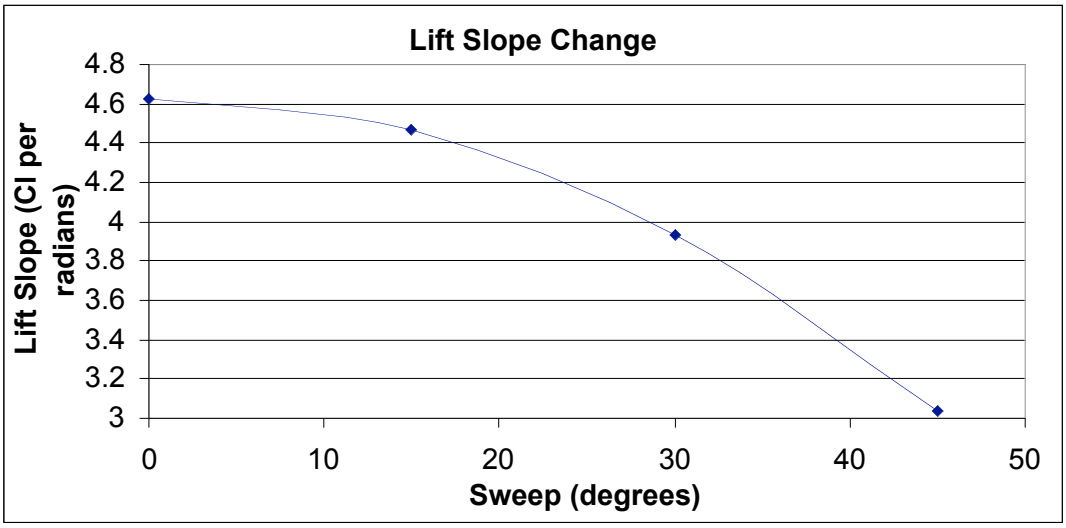

Figure 42. Plot of lift curve slope as a function of wing sweep angle without span extensions.

By observation of the above data, the lift slope decreases as the sweep increases. With increasing sweep, the lift of the aircraft at a certain angle of attack decreases. Therefore, a swept aircraft is capable of reaching a higher angle of attack before stalling. A negative aspect of sweeping to wings is the surface area of the wings is decreased, generating less lift. With increasing sweep, the neutral point and center of gravity both increase.

The same analysis was run with the wing planform with span extensions. The extensions increased the half-span by ten inches; the extension chord is eight inches. The span extension's leading edge is 0.5 inches aft of the wing's leading edge. Figure 43 shows the wing/tail geometry with span extensions at different sweep angles which was used in the program.

The same data was outputted as the analysis conducted on wing/tail configuration without span extensions. Tables 10 and 11 and Figures 44 and 45 show the relationships of center of gravity, neutral point, and lift curve slope to angles of sweep with span extensions.

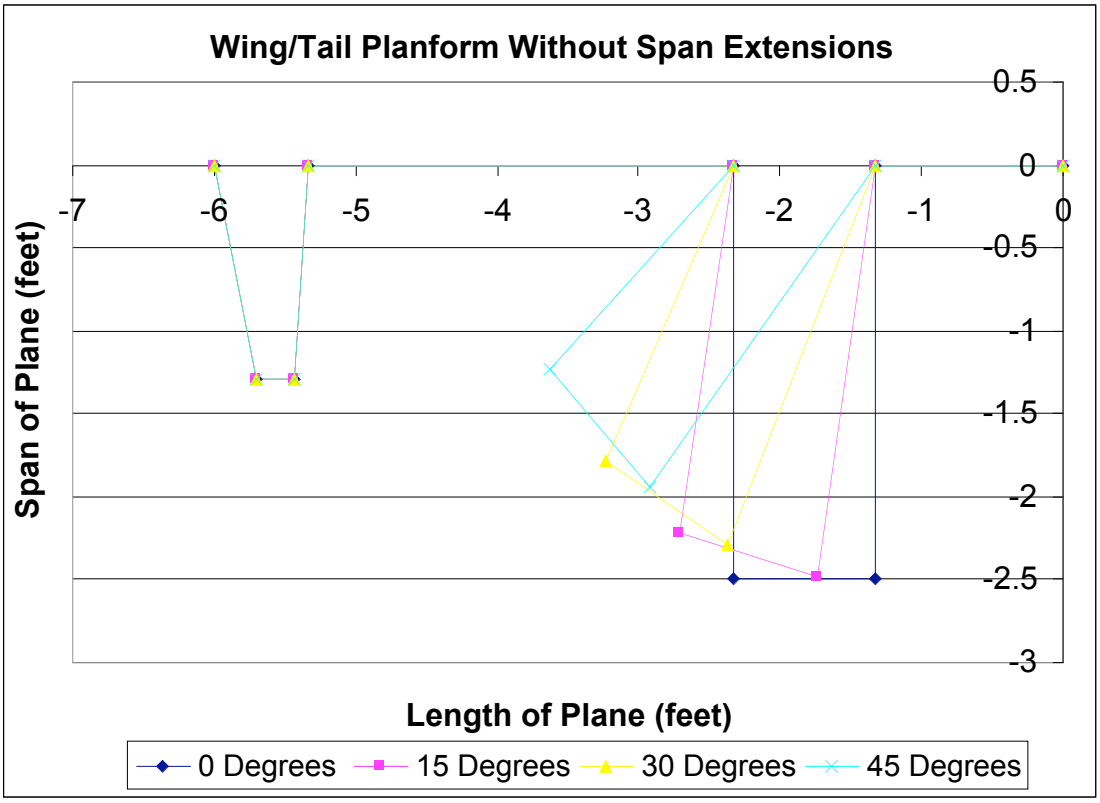

Figure 43. Detailed plot of wing/tail geometry at different sweep angles with span extensions

Table 10. Neutral point and center of gravity as a function of wing sweep angle with span extensions

Neutral Point		Center of Gravity	
Sweep (deg)	NP (feet)	Sweep (deg)	CG (feet)
0	1.9767	0	1.8767
15	2.30238	15	2.20238
30	2.60619	30	2.50619
45	3.0095	45	2.9095

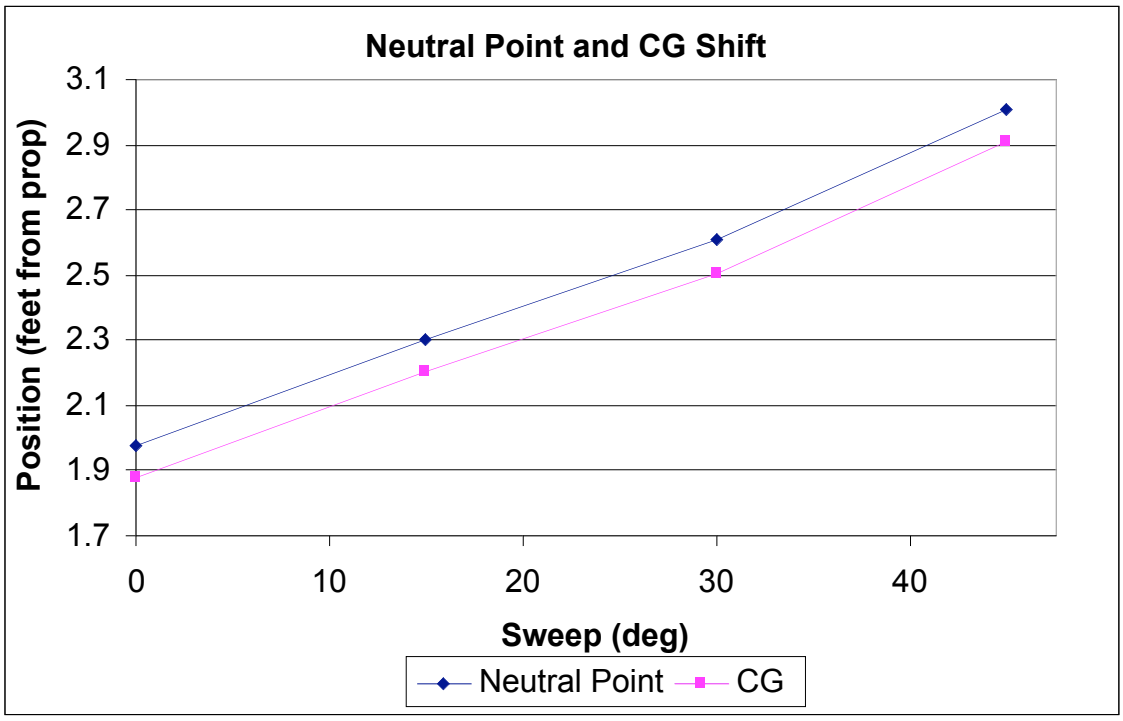

Figure 44. Plot of neutral point and center of gravity shift with wing sweep angle with span extensions. Noting the center of gravity is 10% MAC stable.

Table 11. Lift curve slope as a function of wing sweep angle with span extensions

Lift Slope	
Sweep (deg)	Lift Slope (Cl per radians)
0	6.3661
15	5.64637
30	5.10636
45	4.17351

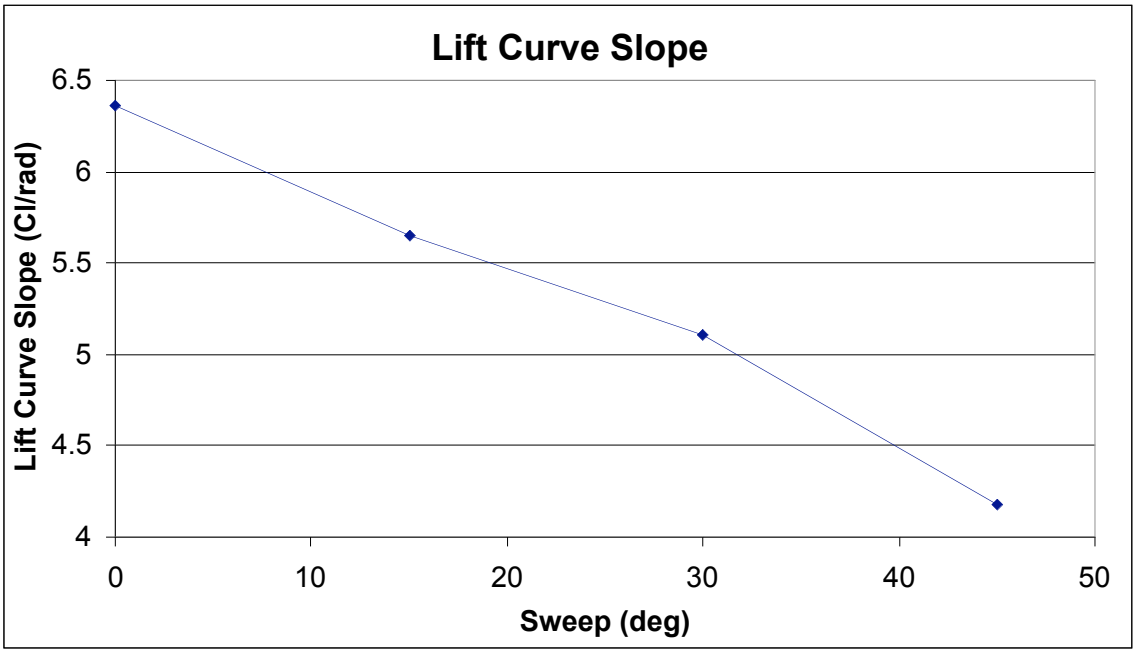

Figure 44. Plot of lift curve slope as a function of wing sweep angle with span extensions.

A comparison between wing/tail configurations with and without span extensions data was constructed. The plots seen in Figures 46 and 47 show the comparison of the lift curve slope and neutral point as a function of sweep through both configurations. The lift curve slope with the span extensions is much higher at all points. As is expected, more lift is produced with more wing area. The neutral point at zero degrees sweep on the configuration with extensions is further forward than the configurations without extensions. As sweep increases, the neutral point of the configuration with extensions is further back than the configuration without extensions.

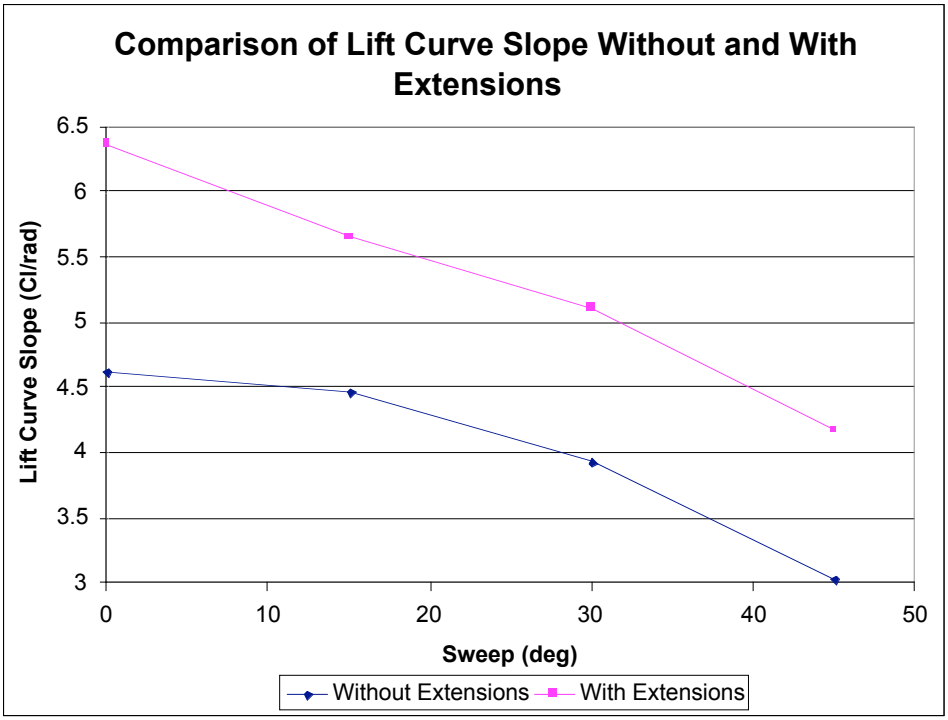

Figure 46. Comparison plot of lift curve slope as a function of wing sweep angle with and without span extensions.

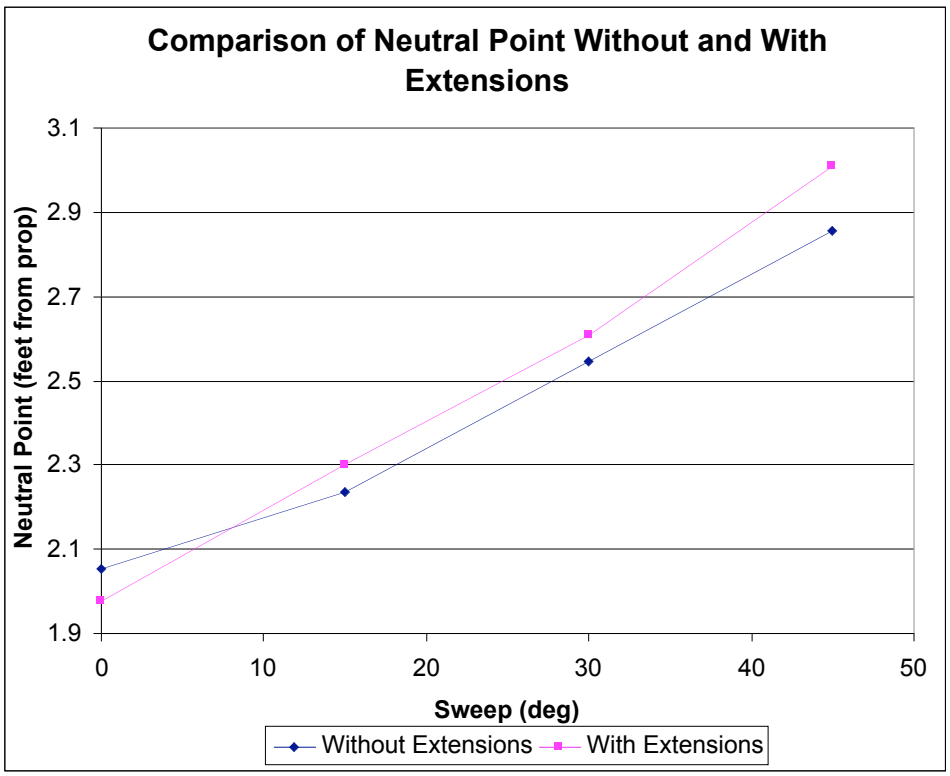

Figure 47. Comparison plot of neutral point as a function of wing sweep angle with and without span extensions.

Tornado Results. Theoretical analysis was also completed on the aircraft using a vortex lattice code known as Tornado. Overall, five configurations were examined: plain wing geometry, wing extensions out, 15 degrees of wing sweep, 30 degrees of wing sweep, and 45 degrees of wing sweep. For the purposes of this analysis, the wing extensions are not extended while the wings are swept. In all of the configurations, the tail geometry was also included in the modeling. For the analysis, two separate airspeeds were studied: 17 m/s and 27 m/s. Additionally, the team used a flat plate analysis because the aircraft's airfoils are not parallel to the flow when sweeping the wings. This presented a problem when using a cambered line because Tornado swept the wings back in a manner so that the airfoils did stay parallel to the flow. Examples of the wing geometry can be found in Figures 48 and 49.

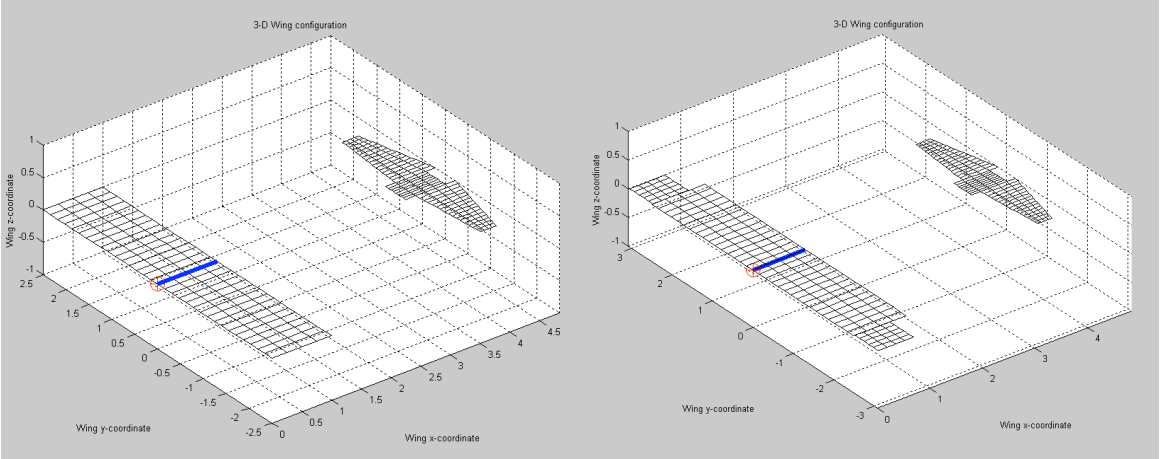

Figure 48. The plain geometry can be seen modeled on the left hand side. The right hand side shows the wing extensions modeled.

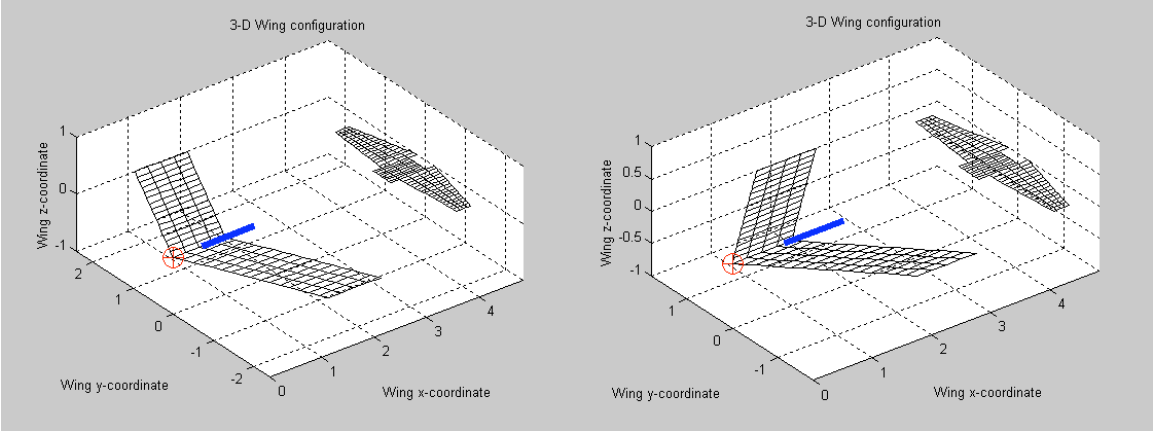

Figure 49. This figure represents the swept aircraft geometry conditions. On the left, one can see a wing sweep of 15 degrees. On the right, one can see a wing sweep of 45 degrees. A third case of 30 degrees was also completed, but is not shown here.

For each of the aircraft configurations, the aircraft was placed through an alpha sweep calculation where the angle of attack was varied from -10 degrees to 20 degrees in increments of 5 degrees. At each angle of attack, lift, drag, and moment coefficients were computed. At the end, these coefficients were plotted against angle of attack. The team took the slope of each of these lines to get a sense of the aircraft's stability. The $dCl/d\alpha$ and $dCm/d\alpha$ is outlined in Table 12. From these results one can see that the aircraft is stable in all configurations because $dCl/d\alpha$ is positive and $dCm/d\alpha$ is negative. Additionally, one can see that the change in airspeed did not affect our results. Also, with wing extensions the $dCl/d\alpha$ increased and $dCm/d\alpha$ decreased. This makes sense because lift should increase with additional wing area, also causing for a more negative moment coefficient—an observation is consistent with that from VLMpc. Moreover, as the wings sweep back $dCl/d\alpha$ and $dCm/d\alpha$ decreased. Furthermore, the Cm vs. angle of attack graph stayed constant for all aircraft configurations and velocity speeds. This graph can be seen in Figure 50.

Table 12. $dCl/d\alpha$ and $dCm/d\alpha$ for various aircraft configurations and velocities.

Configuration	17 m/s		27 m/s	
	$dCl/d\alpha$	$dCm/d\alpha$	$dCl/d\alpha$	$dCm/d\alpha$
Plain	5.0	-4.4	5.0	-4.4
Extensions	6.0	-4.7	6.0	-4.7
Sweep: 15 deg	4.5	-6.5	4.5	-6.5
Sweep: 30 deg	4.4	-6.9	4.4	-6.9
Sweep: 45 deg	4.1	-8.3	4.1	-8.3

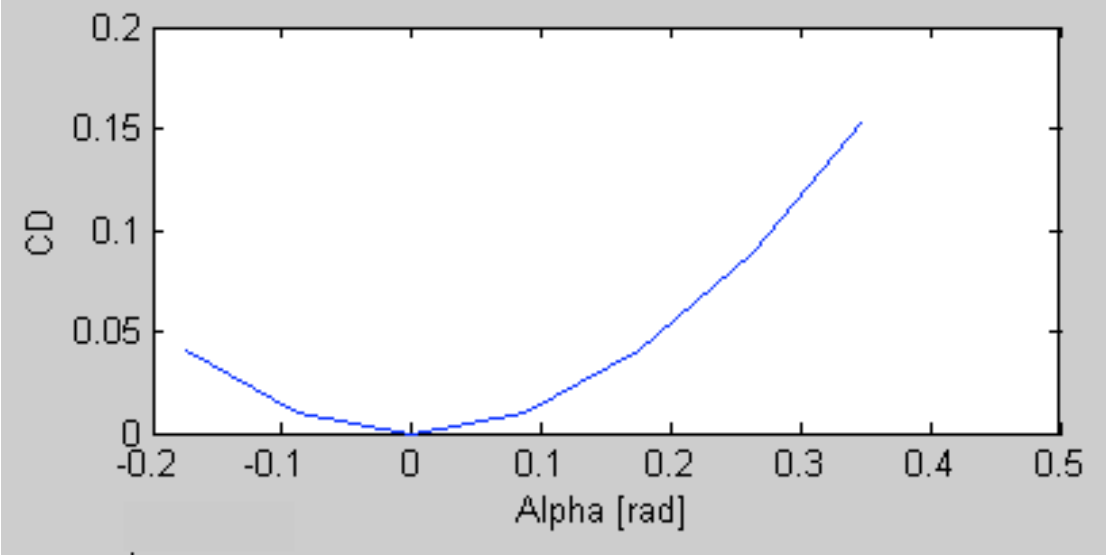

Figure 50. Coefficient of Drag vs. Angle of Attack.

USAF DATCOM Results. A major obstacle the team encountered in last semester's design centered around a lack of data analyzing stability and control values. In working with the POS the team learned from experience that control surfaces that are not carefully sized can result in erratic and unpredictable flight. During the design process, one of the more challenging factors was designing an elevator that was capable of providing adequate longitudinal control over a variety of wing sweep positions. As the wings sweep back, the center of gravity of the plane shifts aft and the tail and elevator must be designed to compensate for this shift. A second major focus was ensuring the plane maintained adequate

roll control through all configurations. With the POS, the ailerons were initially undersized, and even after relocation of the servos to provide more deflection, we found that the plane had difficulty achieving banked turns. Proper sizing of the ailerons to provide ample roll control in a situation where the wings were extended for loiter flight was another cornerstone of the design. Above all else, the team needed to ensure that the plane would be stable in all configurations so that it could be controlled in flight. This was achieved through careful weight distribution to ensure a center of gravity as close to the quarter chord of the wing as possible and monitoring of static margin during sweep. Initial stability and control values were necessary in order to estimate the aircraft's capabilities.

Over the years, a large number of stability and control equations were compiled into a collection known as the United States Air Force Data Compendium. In the mid-1970's, engineers and programmers at Wright Patterson Air Force Base converted these files into a digital program that could be run with Fortran. When geometry and flight conditions are input, Digital Datcom will output static stability derivatives along with high lift and control values. Separate code was input that allowed users to calculate control deflections and hinge moments along with necessary increments for vehicle trim. Over the years many programs have spawned from Digital Datcom such as DAR Corporations Advanced Aircraft Analysis. This program uses the general Data Compendium equations to compute stability and control derivatives as well as several other properties including aerodynamics, performance, and structures. For our stability and control analysis, Advanced Aircraft Analysis was the tool of choice.

During the initial phase of collecting and inputting the geometry of the plane, some approximations were necessary. To account for the open space created by the tail booms the fuselage was modeled as a rectangular box in the front portion of the plane. The segment leading

to the tail had to be designed as a single plank, tapering in height from the fuselage to the tail. This raised some concern due to the fact that this geometry did not take into account the ability for air to flow through the tail booms.

The main objective of this analysis was to get a collection of data detailing the stability of the plane and effectiveness of control surfaces compared against those of a stable plane. A comparison of our plane in both unswept and fully swept positions to a Cessna 208 is shown in Table 13. The Cessna 208 is a dependable small cargo plane with ordinary flight characteristics. Stability and control derivatives are presented for all control surfaces as well as the overall values for the plane. The plane was analyzed in both wing positions to see if the sweep angle would have any detrimental effects on the control of the plane.

Table 13. Stability and Control Derivative Values.

*Assume all Values are in rad^{-1} (unless noted)	Unswept	45 Degree Sweep	Cessna 208	Explanation
Angle of Attack Derivatives				
C_{L_α}	5.8022	4.0957	5.8706	Lift coefficient as a function of angle of attack
C_{D_α}	0.8972	0.6278	0.2161	Drag coefficient as a function of angle of attack
C_{M_α}	-4.9	-6.5817	-0.7149	Moment coefficient as a function of angle of attack
A.O.A. Rate Derivatives				
$C_{L_{\alpha dot}}$	2.5678	2.4378	2.5726	Lift coefficient due to AOA rate derivative
$C_{D_{\alpha dot}}$	0	0	0	Drag coefficient due to AOA rate derivative
$C_{M_{\alpha dot}}$	-9.1017	-8.6409	-9.6915	Moment coefficient due to AOA rate derivative
Pitch Rate Derivatives				
C_{Lq}	8.836	17.3727	7.7919	Lift coefficient due to rate pitch derivative
C_{Dq}	0	0	0	Drag coefficient due to rate pitch derivative
C_{Mq}	-29.9617	-38.182	-32.3278	Moment coefficient due to rate pitch derivative
Roll Rate Derivatives				
C_{lp}	-0.4219	-0.3635	-0.5494	Rolling moment coefficient due to roll rate derivative
C_{yp}	0	0	-0.0835	Side force coefficient due to roll rate derivative
C_{np}	-0.113	-0.0358	-0.0361	Yawing moment coefficient due to roll rate derviative
Yaw Rate Derivatives				
C_{lr}	0.014	0.0262	0.1122	Rolling moment coefficient due to yaw rate derivative
C_{yr}	0.0303	0.0386	-0.0412	Side force coefficient due to yaw rate derivative
C_{nr}	-0.2242	-0.2294	-0.0092	Yawing moment coefficient due to yaw rate derivative
Elevator Control Derivatives (at 45 degrees)				
$C_{D_{\delta e}}$	0.0069	0.0069	0.0245	Drag coefficient due to elevator delfection derivative
$C_{L_{\delta e}}$	0.2395	0.2395	0.662	Lift coefficient due to elevator deflection derivative
$C_{M_{\delta e}}$	-0.847	-0.847	-2.5096	Moment coefficient due to elevator deflection derivative
$C_{h_{\delta e}}$	-0.66	-0.66		Elevator Hingemoment due to elevator deflection derivative
Rudder Control Derivatives				
$C_{y_{\delta r}}$	0.046	0.046	0.1934	Side force due to rudder deflection derivative
$C_{l_{\delta r}}$	-0.0028	-0.0028	0.0162	Rolling moment due to rudder deflection derivative
$C_{n_{\delta r}}$	-0.037	-0.037	0.0192	Yawing moment due to rudder deflection derivative
Aileron Control Derivatives				
$C_{y_{\delta a}}$	0	0	0	Side force due to aileron deflection derivative
$C_{l_{\delta a}}$	0.0525	0.0414	0.1578	Rolling moment coefficient due to aileron deflection derivative
$C_{n_{\delta a}}$	-0.001	-0.0007	-0.0082	Yawing moment coefficient due to aileron deflection derivative

Figures 51-54 show the control effectiveness of MWP-06. In reviewing the control effectiveness, the only area of major concern is the capabilities of the ailerons to create an ample roll moment. Our plane will maneuver, but perhaps not at the rate we had initially desired. The elevator proved to be very effective; the program states that it is capable of changing the plane's angle of attack by 19 degrees when deflected at 45 degrees. This is a welcome departure from the values the POS provided. The rudder is ample for providing the necessary yaw the plane will need.

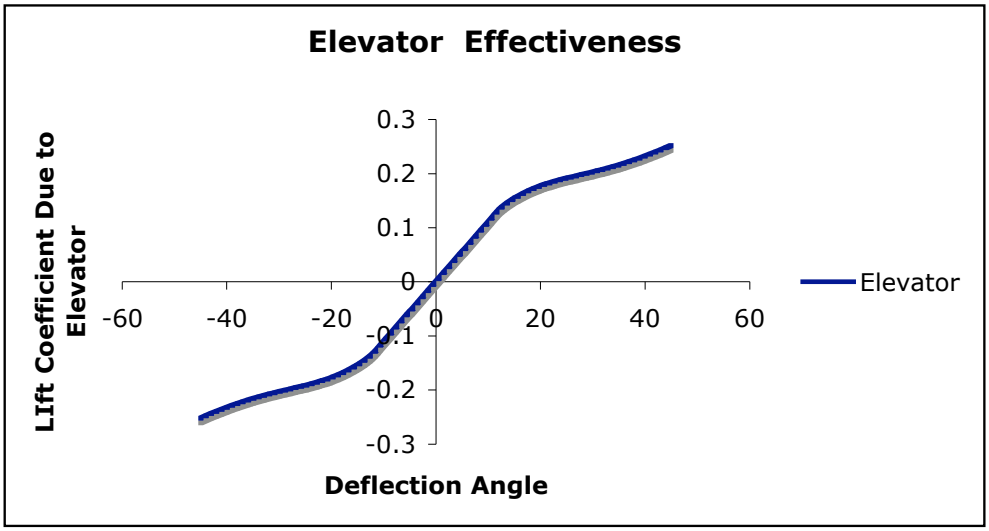

Figure 51. The effectiveness of the elevator when the wings are unswept. Elevator lift coefficient versus deflection angle.

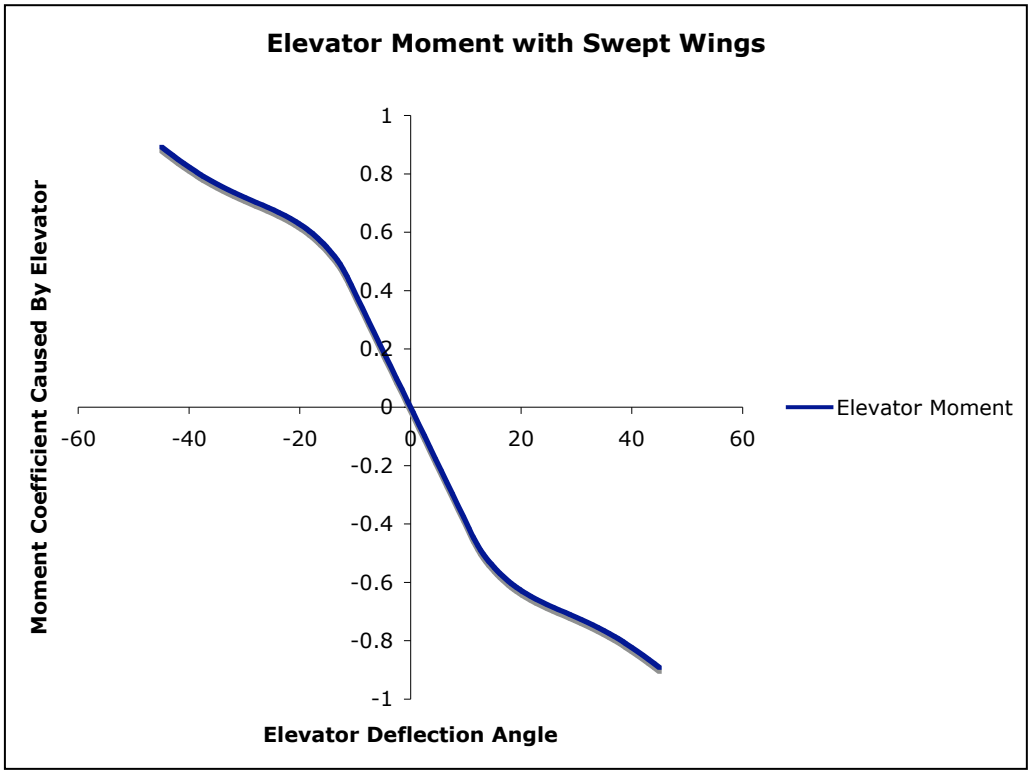

Figure 52. The effectiveness of the elevator when the wings are swept. Elevator moment coefficient versus deflection angle.

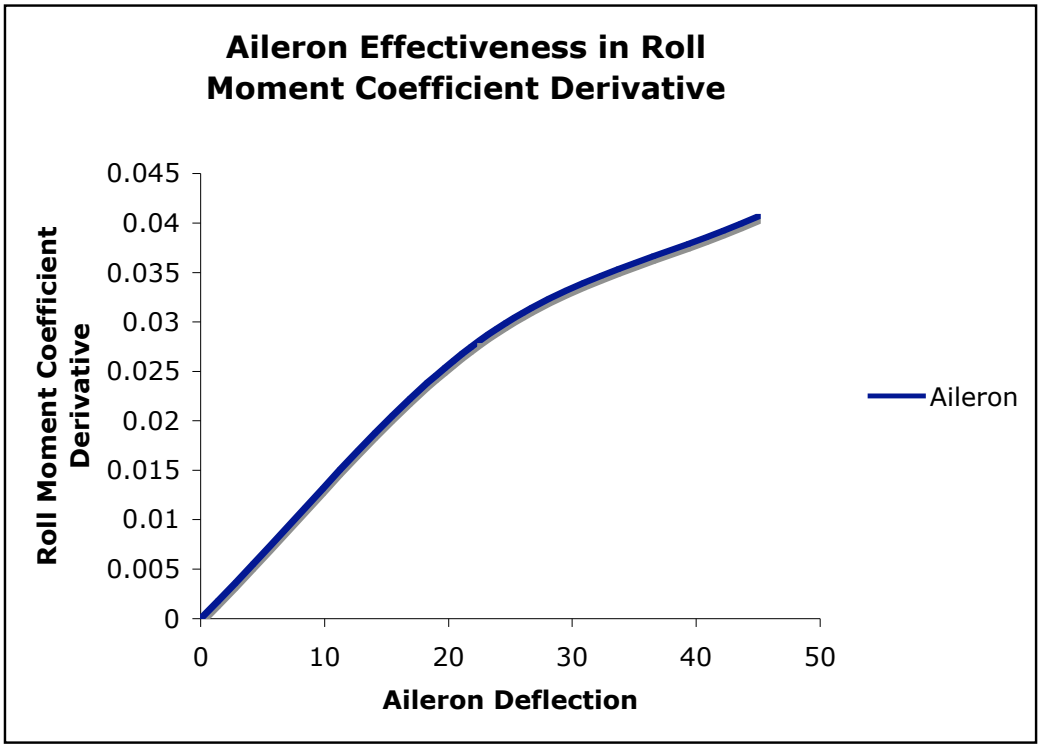

Figure 53. Aileron effectiveness in roll moment coefficient derivative. Roll moment coefficient derivative versus aileron deflection.

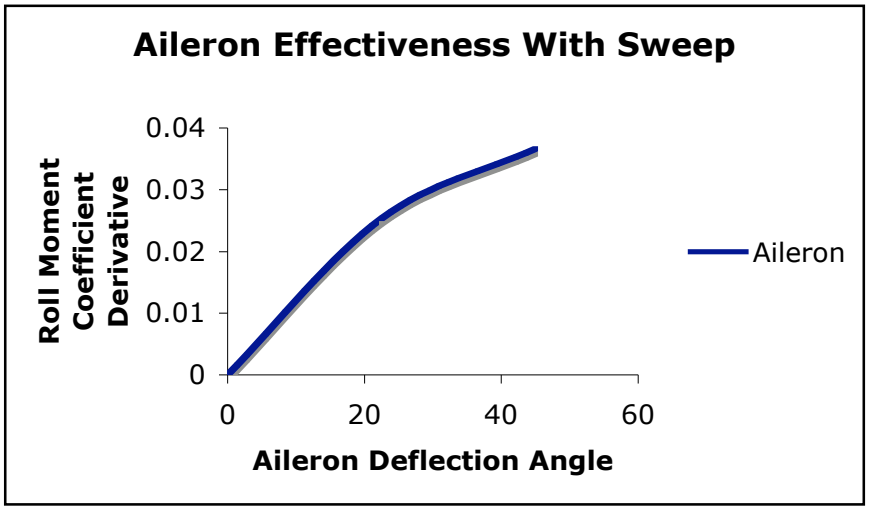

Figure 54. Aileron effectiveness with sweep. Roll moment derivative coefficient versus deflection.

Mass Balance

In order to achieve flight, it is important to determine where the center of gravity of the plane lies. This was done by performing a mass balance on MWP-06's components. A major assumption in this process allows for the estimation of all the components as point masses at their individual centers of gravity. Using this technique, the plane was balanced about two axes.

To determine if MWP-06 was symmetrical, the plane was balanced across the centerline of the fuselage. The distance from the center line of the plane to each point mass was measured. Then, by summing the product of the weight of each component times that distance and dividing by the total mass, the center of gravity of the plane was found. This value was found to be 0.0006 inches from the centerline of the fuselage. This distance was deemed negligible in the overall system; therefore, MWP-06 is symmetrical.

The second axis about which the CG was determined was as a distance from the tip of the propeller. Using the same mathematical technique, the CG in this direction was found to be 22 inches from the tip of the propeller. The landing gear was placed using this information.

Final Status of MWP-06

MWP-06 has been fully assembled and all morphing abilities are functioning. The team had planned to test the plane in the wind tunnel. However, due to revised sizing specifications made after our single-degree-of-freedom test on the POS, our plane was deemed too large for the strut and sting wind tunnel mounts. A tentative flight is scheduled before graduation.

Lessons learned: A brief map of landmines to sidestep

Above all else, it was the desire of the team to create a finished product that was innovative by comparison to all previous years. To accomplish this, we incorporated the use of composite materials, an area with a very steep learning curve, into the wing design. Furthermore, we explored both the application of new morphing actuation and the more efficient implementation of previous methods. Along the way, there were serious setbacks that, under the time constraints of the spring semester, led to undue stress. By application of the law of 20-20 hindsight, many of the delays could have been avoided. The purpose of this section is to outline some of the major issues of the semester in hopes that future teams may avoid them and push their own project to new levels.

The task of working with composite materials should not be underestimated. Long before construction began, it was understood that though stronger, lighter, and overall a better construction material, carbon fiber would be difficult to work with. In addition to the task of locating a distributor who actually had the material in stock to sell, construction of the foam core mold must be considered. First, there is no need to split the core into two sections, one hollowed and the other solid. The strength of the wings is in the carbon, and once laid, the section housing the extension can be hollowed out as designed. By keeping one solid airfoil, the imperfections introduced by high pressure vacuum bagging can be avoided. Second, keep an open mind

towards outsourcing the cutting of the foam core. Though it is no longer necessary to hollow out a section of the core, the main problem with this year's design, the inaccuracies of using a hot wire on a more complex airfoil shape are still present, and could be problematic. Not only will the finished outsourced product be perfect to specification, but the many hours spent trying to master the hotwire can be saved.

Locate someone with knowledge of vacuum bagging and composite materials and become their friend. As mentioned before, the learning curve for working with composites is very steep. No amount of reading on the internet will replace the hands on experience you gain by actually working with it. Also, having someone with experience around to answer questions is of great benefit. This additional experience may prevent costly mistakes from being made.

Unlike wings constructed with balsa and Monokote®, every cut in a body covered in carbon fiber is final and will very likely compromise the strength of the material. Plan every modification, check every measurement, and be patient in the final stages of construction to avoid mistakes. Though holes in the wing are a necessity, placement of servos, switches, and other hardware should be accomplished as non-invasively as possible.

Although complications with wing construction accounted for most of the delays, the team had other difficulties. In depth structural analysis and testing should be completed before the construction of a model. Also, test facility availability should be checked far in advance. This includes notifying wind tunnel officials of the overall plane span and length. Finally, there must be equal division of labor in any project; no one subgroup should be left with the brunt of the work. Furthermore, there must be an understanding that when one subgroup's work is completed, efforts must be focused elsewhere on the project as long as other team members are

still working. A project cannot be completed a timely manner without the combined efforts of the entire team.

Though a few of the biggest problems we experienced have been outlined here, there is no way to avoid all delays. Periods of downtime should be planned into the construction schedule, and more time in addition to this should be expected. Though every attempt to meet construction deadlines should be made, allowing extra cushion on major deadlines will improve team efficiency during the final construction rush.

Conclusion

At the start of this year, the 2005-2006 Morphing Wing Senior Design Team was given two tasks: rebuild and fly the POS and design, build, and fly a new plane. During the Fall 2005 semester, the team rebuilt, analyzed, experimentally and theoretically tested, and flew the POS. This semester, the team completed repairs on the POS, performed a single-degree-of-freedom wind tunnel experiment, and flew again in Salem, VA. In addition, the team successfully designed and built MWP-06. In addition, analysis was completed on our new plane using three validation codes: VLMpc, Tornado, and USAF DATCOM. A plan is in place to fly MWP-06 before graduation. The lessons learned from this year's Morphing Wing Senior Design Team will aid in future design projects.

References

B-1B Lancer. Federation of American Scientists. 2 May 1997. 12 December 2005. <http://www.fas.org/nuke/guide/usa/bomber/b-1.htm>.

F-111. Federation of American Scientists. 24 December 1998. 12 December 2005. <http://www.fas.org/man/dod-101/sys/ac/f-111.htm>.

F/A-18 Hornet. Federation of American Scientists. 25 April 2000. 12 December 2005. <http://www.fas.org/man/dod-101/sys/ac/f-18.htm>.

Etkin, Bernard. Dynamics of Flight: Stability and Control. John Wiley and Sons, Inc., 1996.

Franklin Institute Online, The. 8 December 2005. <http://www.fi.edu/time/Journey/Time/Escapements/rackpinion.gif>.

Morphing Wing Team Formal Report, Fall 2005.

Raymer, D.P. Aircraft Design: A Conceptual Approach. AIAA Education Series, 1989.

Senior Aircraft Design Reports. "AEME Morphing 2002-2003 Final Reports – Spring Report." May 2003. 12 December 2005. <http://www.aoe.vt.edu/~mason/Mason_f/MorphS03Rpt.pdf>.

Senior Aircraft Design Reports. "AEME Morphing 2004-2005 Final Reports – Fall Report." December 2004. 12 December 2005. <http://www.aoe.vt.edu/~mason/Mason_f/MorphF04Rpt.pdf>.

Senior Aircraft Design Reports. "AEME Morphing 2004-2005 Final Reports – Spring Report." May 2005. 12 December 2005. <http://www.aoe.vt.edu/~mason/Mason_f/MorphS05Rpt.pdf>.

Software for Aerodynamics and Aircraft Design (W.H. Mason, Virginia Tech), Modified January 31, 2006 http://www.aoe.vt.edu/~mason/Mason_f/MRsoft.html

Swing-wing. Wikipedia, the Free Encyclopedia. 24 October 2005. 8 December 2005. <http://en.wikipedia.org/wiki/Swing-wing>.

USAF Stability and Control Digital Datcom, Volumes 1-2. Technical Report AFFDL-TR-79-3032. Wright Patterson Air Force Base, August 1977-November 1978.

USAF Stability and Control Digital Datcom, Volume 2: Implementation of Methods. AFFDL-TR-76-45, March 1975-March1976.

U.S. Forest Service Research Note. Forest Product Laboratory, Forest Service, US Department of Agriculture. "Bending Strength and Stiffness of Plywood." September 1964. <http://www.fpl.fs.fed.us/documnts/fplrn/fplrn059a.pdf#search='Plywood%20Material%20Properties>.

Weiss, Peter. "Wings of Change." Science News Online. 6 December 2003. 12 December 2005. <http://www.sciencenews.org/articles/20031206/bob9.asp>.

Young's Modulus. Wikipedia, the Free Encyclopedia. 15 October 2005. 12 December 2005. < http://en.wikipedia.org/wiki/Modulus_of_elasticity>.